Detection of Magma Reservoir beneath the Changbaishan Volcanic Region through Seismic Ray Tracing

Annual Report 01 for
DOS Contract No. 19AQMM20P0737 (BAA-2020-DOS-AVC-001)
May 1, 2020 to April 30, 2021

June 15, 2021

Prepared By
Dr. Youlin Chen
Array Information Technology
Advanced Technology Division
5130 Commercial Dr. Suite B
Melbourne, FL 32940
Phone: (617) 959-0478
youlin.chen@arrayinfotech.com

For

United States Department of State

Bureau of Arms Control, Verification and Compliance

2201 C Street, N.W., RM 5725 (AVC/VPO)
Washington, DC 20520

APPROVED FOR PUBLIC RELEASE; DISTRIBUTION UNLIMITED

REPORT DOCUMENTATION PAGE

Form Approved
OMB No. 0704-0188

1. REPORT DATE *(DD-MM-YYYY)*	**2. REPORT TYPE**	**3. DATES COVERED** *(From - To)*
15-06-2021	Annual Report 01	1/5/2020 – 30/4/2021

4. TITLE AND SUBTITLE

Detection of Magma Reservoir beneath the Changbaishan Volcanic Region through Seismic Ray Tracing

5a. CONTRACT NUMBER
19AQMM20P0737

5b. GRANT NUMBER

5c. PROGRAM ELEMENT NUMBER

6. AUTHOR(S)

Youlin Chen

5d. PROJECT NUMBER

5e. TASK NUMBER

5f. WORK UNIT NUMBER

7. PERFORMING ORGANIZATION NAME(S) AND ADDRESS(ES)

Array Information Technology, Inc.
7074 Greenway Center Drive, Suite 600
Greenbelt, MD 20770-3574

8. PERFORMING ORGANIZATION REPORT NUMBER

9. SPONSORING / MONITORING AGENCY NAME(S) AND ADDRESS(ES)

United States Department of State
Bureau of Arms Control, Verification and Compliance
2201 C Street, NW
Washington, DC 20520

10. SPONSOR/MONITOR'S ACRONYM(S)

U.S DOS/AVC

11. SPONSOR/MONITOR'S REPORT NUMBER(S)
AVC-VTN-21G05

12. DISTRIBUTION / AVAILABILITY STATEMENT

Public Release Approved; Distribution Unlimited.

13. SUPPLEMENTARY NOTES

14. ABSTRACT

The "big mantle wedge" model for the Changbaishan (CBS) volcano predicts a magma reservoir underneath this volcano. To detect and study this magma reservoir, we judiciously select 73 deep earthquakes near the CBS and analyze the seismograms of these events recorded at eight temporal and permanent seismic networks in NE China. We propose to perform extensive ray tracing simulations for these deep earthquakes to determine the location, range, and degree of melt of the magma reservoir. In the first-year technical progress period, we retrieve all required seismograms, pick P- and S-arrivals, and detect P-wave delays and S-wave shadows. We then start ray tracing simulations with 1D models. Our initial results show that a low-velocity anomaly exists in a large area beneath the CBS volcano.

15. SUBJECT TERMS
Volcano, P-wave delay, S-wave shadow, Complete ray tracing

16. SECURITY CLASSIFICATION OF: UNCLAASIFIED			**17. LIMITATION OF ABSTRACT**	**18. NUMBER**	**19a. NAME OF RESPONSIBLE PERSON** Rongsong Jih
a. REPORT UNCLASSIFIED	**b. ABSTRACT** UNCLASSIFIED	**c. THIS PAGE** UNCLASSIFIED	SAR	34	**19b. TELEPHONE NUMBER** *(include area code)* 1-202-647-8126

Standard Form 298 (Rev. 8-98)
Prescribed by ANSI Std. Z39.18

EXECUTIVE SUMMARY

The active intraplate Changbaishan (CBS) volcano is most likely originated from the upwelling of hot and wet asthenospheric materials in the mantle above the stagnant Pacific slab in the mantle transition zone. It thus predicts a magma reservoir/chamber existing beneath the CBS. Many previous studies suggested low-velocity anomalies in the lower crust or upper mantle and even partial melt of lower crust beneath the CBS volcano; however, those studies did not provide direct evidence of the existence of magma reservoir due to the insufficient model resolution limited by the used data and techniques. We propose to detect the magma reservoir beneath the CBS through 1D and 3D ray tracing simulations. The feasibility of our method benefits from abundant seismographs of deep-focus earthquakes that occurred within the Wadati-Benioff seismic zone of the subducting Pacific slab that were recorded at various seismic stations densely distributed in NE China. The seismic rays leaving the deep-focus earthquakes and arriving at the stations can fully scan the crustal and upper mantle area underneath the CBS volcanic region. If a low-velocity anomaly exists, P-wave delays and S-wave shadows are expected to be observed on these stations. The comprehensive 1D and 3D ray tracing simulations allow us to determine ray patterns and their sensitivities to the variations in velocity structure, hence to detect the magma reservoir/chamber beneath the CBS volcano and to determine its position, size and degree of melt that can explain the observed P-wave delays and S-wave shallows. This study will reveal the detailed crustal and upper mantle structure beneath the CBS volcanic region and reconcile the debates for the origin and Earth structure of volcanoes in Northeast Asia.

The main tasks finished in the first-year technical progress period include:

1. *Seismic Data Collection*: We judiciously select 73 deep-focus earthquakes with the minimum magnitude 4.5 and make use of their seismograms recorded at five temporal seismic networks (1U, XI, XL, YP, and V0) and three permanent networks (HL, JL, and LN) deployed in NE China. Networks 1U, XI, XL, and YP belong to PASSCAL seismic deployments, and we download the waveform data from the IRIS-DMC. Permanent networks HL, JL, and LN are part of the Chinse National Digital Seismic Network (CNDSN) and the temporal network V0 belongs to the Chinarray. The waveform data of the four Chinese networks are retrieved from the Chinese Earthquake Network Center (CENC) and the Institute of Geophysics, CEA, respectively, through the collaboration program between ARRAY and Chinese collaborators.

2. *Data Processing*: Besides the routine data processing for seismograms, such as base-line removal, filtering, and data quality control, we manually pick P- and S-wave arrivals whenever applicable. These observed arrivals will be compared to the theoretical predictions from ray tracing simulations. On some stations, the S-waves are missing or too weak to be identified.

3. *P-wave Delays and S-wave Shadows*: We have observed P-wave delays and S-wave shadows on many stations. The S-wave shadow is quantified by the ratio of S/P amplitudes. The stations showing S-wave shadows concentrate around the CBS volcanic region and extend to a large area in NE China.

4. *Complete Ray Tracing*: We employ the Complete Ray Tracing (CRT) method [Červeny et al., 1988] to perform 1D and 3D ray tracing simulations. The CRT program involves many input parameters to construct a 3D model and control the ray tracing computation. It provides high flexibility in computing seismic rays, but also takes us time to understand and configurate these input parameters. We have performed the first ray tracing simulation for our problem using the

1D global AK135 model. Our observations along with the conclusions derived from previous studies provide us the knowledge to determine the parameters for the CRT program. Many stations surrounding the CBS volcanic region show P-wave delays as large as 3 – 5s, indicating that such delays are caused by a low-velocity anomaly beneath the CBS volcano.

TABLE OF CONTENTS

1 INTRODUCTION

1.1 Background

The Changbaishan (CBS, or Mt. Paektu called in Korea) volcano is the largest volcano in NE Asia, straddling the border between Jilin province, NE China, and North Korea (The Democratic People's Republic of Korea). It has been reported that CBS erupted many times in history, such as in BC 1120, AD 1050, 1413, 1597, 1668, 1702, and 1903, although some eruptions were skeptical [Kang et al., 2011]. An episode of unrest from 2002 to 2005, characterized by significantly increased seismicity with shallow focal depth (< 5km), ground deformation with Mogi source at 2 to 6km measured by GPS, fluid geochemical anomalies, and emission of volcanic gases [e.g., Xu et al., 2012; Wei et al., 2013] showed the CBS volcano continues to be active.

Since the CBS volcano lies far from any tectonic plate boundary, it is difficult to explain this intraplate volcano using the plate tectonic paradigm. Some researchers suggested that the CBS volcano was originated via either the accretion processes at the craton margin since Meso-proterozoic or due to the subduction processes of the Pacific plate into the eastern Eurasia continental margin before the opening of the Japan Sea [e.g., Zhang and O'Reilly, 1997]. Turcotte and Schubert [1982] assumed that the CBS volcano could be a hotspot like the Hawaiian-Emperor volcanoes chain, while Tatsumi et al. [1990] considered it to be a kind of back-arc volcano. A deep mantle plume rooted in the base of the lower mantle seems an unlikely source for CBS volcano in that there is no slow seismic anomaly in the lower mantle indicative of mantle upwelling, no evidence for a flood basalt indicating the arrival of a plume head, or no hotspot track associated with the volcanism either.

Recently, more and more studies indicated that the origin of this intraplate volcano is associated with the upwelling of hot and wet asthenospheric materials in the big mantle wedge above the stagnant part of the Pacific slab lying horizontally in the mantle transition zone (410-660km depth) beneath the Korean Peninsula [e.g., Zhao and Tian, 2013]. In this "big mantle wedge" model, dehydration occurs in the transition zone and results in compositional buoyant material rising, causing melting in the uppermost mantle. Many geophysical studies have been made to probe the underlying structure of CBS, including the magnetotelluric measurements [Qiu et al., 2014; Tang et al., 2001], wide-angle reflection and refraction using controlled sources [Zhang et al., 2002; Liu et al., 2005; Song et al., 2007], attenuation [Wu et al., 2006], receiver functions [Hetland et al., 2004; Tao et al., 2014; Ri et al., 2016; Wu et al., 2009; Zhu et al., 2019; Hammond et al., 2020], surface waves [Li et al., 2012; Kim et al., 2017; Yang et al., 2019; Zhu et al., 2019], and teleseismic tomography [Lei and Zhao, 2005; Huang and Zhao, 2006]. These studies using multidisciplinary approaches have identified zones of high conductivity, high attenuation, and low seismic velocity, which in turn were interpreted as indicators of partial melt and/or high temperatures in the crust beneath CBS.

1.2 Review of Previous Studies about the CBS Volcano

Using about one million P-wave travel times of teleseismic events, Huang and Zhao [2006] obtained a high-resolution P-wave velocity tomographic model of the crust and mantle under China and surrounding regions. Under the intraplate CBS volcanic areas, low-velocity zones exist from the surface down to 200-300km depth, right above the mantle wedge of the Pacific subduction slab (Figure 1). Similarly, a regional P-wave velocity tomography generated using teleseismic events data [Lei and Zhao, 2005] also shows low-velocity zones beneath the CBS volcanic areas

(Figure 2). The low-velocity zones extend to an even deeper depth approaching the 410km discontinuity. The P and S tomography images for NE China using waveforms recorded at NECESSArray (YP in Figure 8) and CNDSN stations (Figure 8) [Tang et al., 2014] clearly show a cylinder-shaped low-velocity anomaly from 700km depth to below CBS (Figure 3). The low-velocity anomaly revealed by these studies is a manifestation of mantle upwelling that results in decompression melting producing the observed magmatism of the CBS volcano. Due to the limited resolution of these velocity images, however, they could not confirm that a magma reservoir that was caused by the mantle upwelling exists in the crust or upper mantle. Rather, the structure of the crust and upper mantle is usually determined by the studies using multiple data sets such as receiver functions, controlled source, and surface waves/seismic noise interferometry.

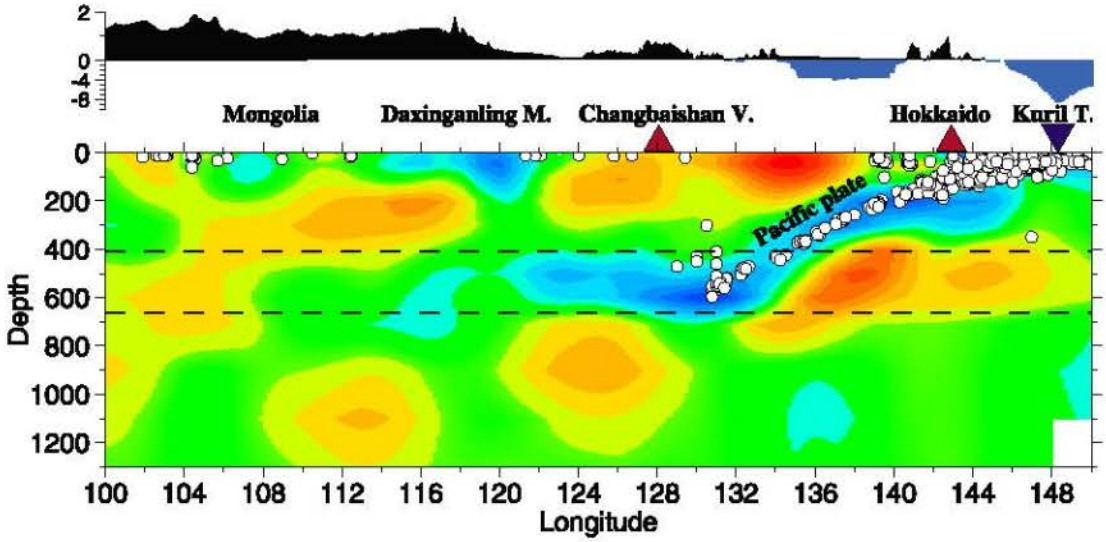

Figure 1. Vertical cross-sections of P wave velocity perturbations along with the profile across the CBS. The white dots indicate earthquakes, the red triangles denote volcanoes, and the dark inverted triangle denotes the Kurl trench. The scale of velocity perturbation is from -2% (red) to 2% (blue). This figure is taken from Figure 8 in Huang and Zhao [2006].

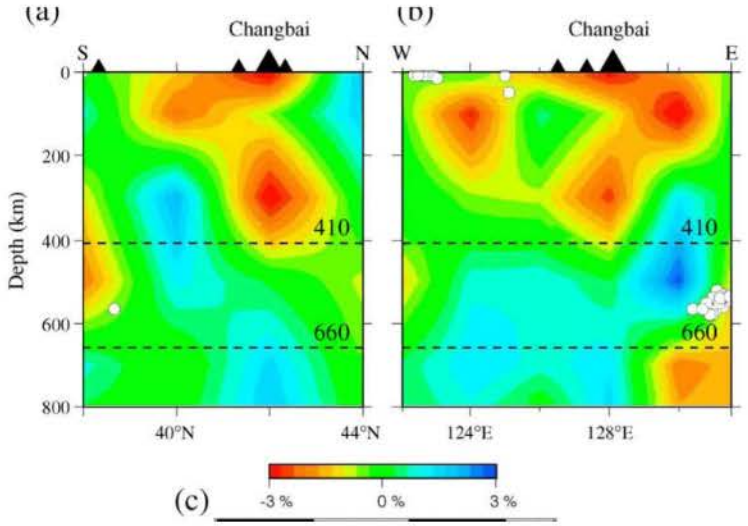

Figure 2. N-S (a) and E-W (b) vertical cross-sections of P wave velocity perturbations across the CBS. The white dots indicate earthquakes, and the black triangles denote the CBS volcano. This figure is taken from Figure 10 in Lei and Zhao [2005].

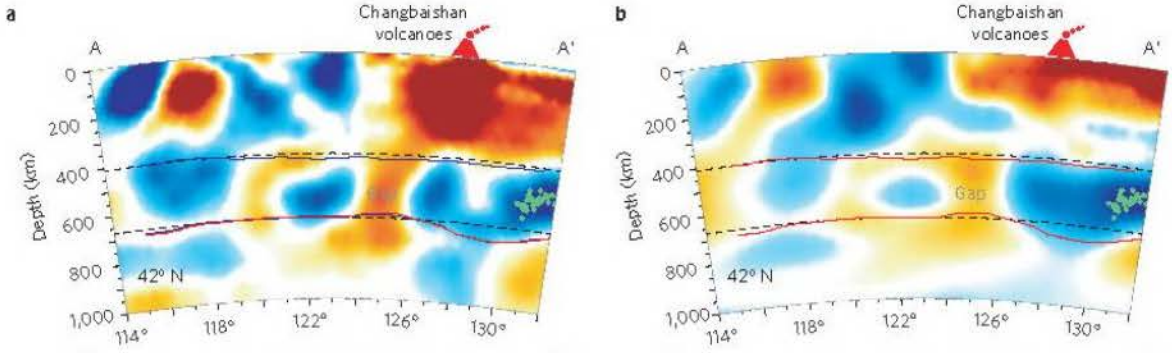

Figure 3. S wave (left panel) and P wave (right panel) velocity perturbations across the CBS. Fast and slow anomalies are indicated by blue and red colors, respectively. Green dots denote deep earthquakes. This figure is taken from Figure 3 in Tang et al. [2014].

As the first-order crustal properties, the crustal thickness (H) and bulk crustal Vp/Vs ratio (κ) beneath the CBS volcano have been estimated in many studies. Applying the H-κ analysis on receiver function data recorded at the seismic deployment of "Study of Changbai Volcanoes and Deep Subduction Zone" (XI in Figure 8), Hetland et al. [2004] resolved a crustal thickness of 30–39km under the volcanic region and 28–32 km away from the volcanic region, with a mid-crust velocity transition at about 10–15 km depth. Using the same data set of XI but by inverting for S-wave profiles from receiver functions, Duan et al. [2005] revealed that the crustal thickness under the crater of CBS volcano (Tianchi) reaches about 36km. Using the seismic deployment of "Mt. Paektu Seismic Network" (1U in Figure 7), Hammond et al. [2020] resolved a thicker crust (up to 40km) beneath the volcano (Figure 4a). The same result was also obtained by Zhu et al. [2019] by performing an H-κ analysis on the different data sets. We plot a 2D relief map showing the crustal thickness in a larger area in NE China surrounding the CBS in Figure 5a. The crustal thickness data are taken from the H-κ search results of (1) Chen and Niu [2016] on the permanent stations in NE China, (2) Hetland et al. [2004] on the temporal network XI, and (3) Ri et al. [2016] and Hammond et al. [2020] on the temporal network 1U. We make use of the results of these studies

because either we own the *H-κ* data [Chen and Niu, 2016] or the *H-κ* data are tabled in the individual research papers. The 2D map is interpolated using the ordinary Kriging method with a minimum smoothness [Chen and Niu, 2016]. The crust beneath the CBS volcano has a thickness of 37 – 38km, about 5km thicker than the crust ~50km away from the volcanic area. Not only the studies using receiver functions [Hetland et al., 2004; Ri et al., 2016; Hammond et al. 2019], but the other studies using multiple data sets such as controlled-source [Liu et al., 2005; Song et al., 2007; Zhang et al., 2002] and surface waves/seismic noise interferometry [Zhu et al., 2019] also reveal a thicker crust presenting beneath the volcano compared to surrounding regions although they may disagree on aspects of the internal crustal structure. A thicker crust is often found beneath volcanic areas linked to the intrusion of mafic material into the lower crust.

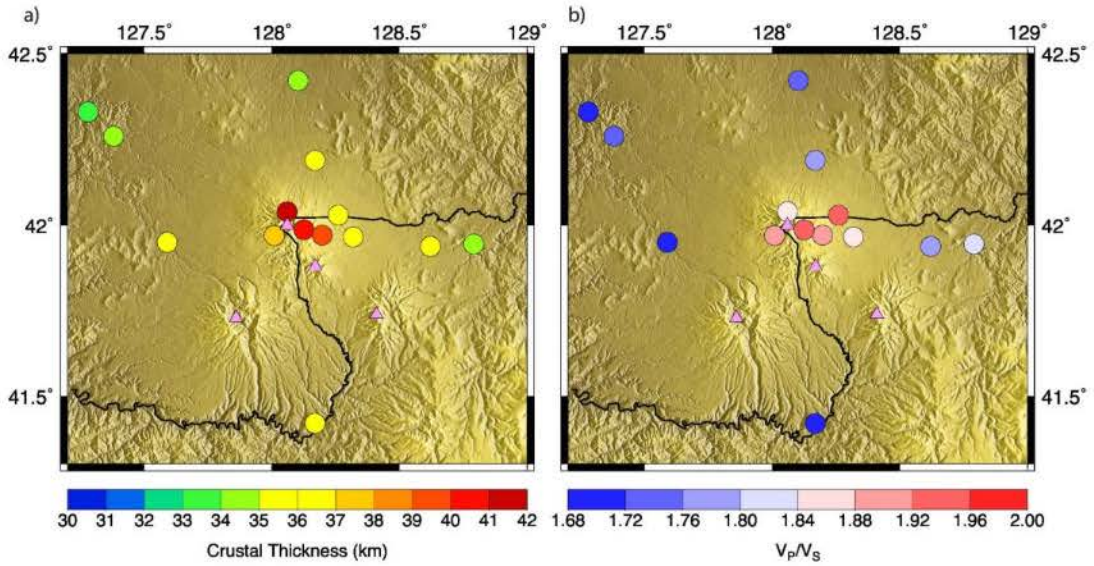

Figure 4. Map of (a) crustal thickness and (b) Vp/Vs ratio around the CBS volcano. The solid circles indicate stations in network 1U. The values of crustal thickness and Vp/Vs ratio derived from individual stations are represented by the colors of solid circles. This figure is taken from Figure 3 in Hammond et al. [2020].

The Vp/Vs ratio estimated by Ri et al. [2016] increases ~20 km from the volcano, rising to >1.87 directly beneath the volcano. Hammond et al. [2020] analyzed more data of the deployment 1U than Ri et al. [2016] did and found that the Vp/Vs ratio can be as high as 1.93 beneath the volcano (Figure 4b). The estimates of Vp/Vs are more ambiguous than the estimates of crustal thickness. Hetland et al. [2004] inferred that the bulk crustal Vp/Vs ratio ranges between 1.63 and 1.87 but suggested that the Vp/Vs ratio is lower under the central volcanic region than under the surrounding areas. We create a 2D Vp/Vs map for a larger region surrounding the CBS using the same sourced data set and method as for the crustal thickness map (Figure 5b). In a region centered at the CBS crater with ~50km radius, the Vp/Vs ratio is generally higher than 1.80, rising to > 1.85 directly beneath the CBS crater. Because only one station (PDBD) used in map Figure 4b has Vp/Vs ratio approaching 1.93 [Hammond et al. 2020], this high value is mitigated during the interpolation process used for Figure 5b.

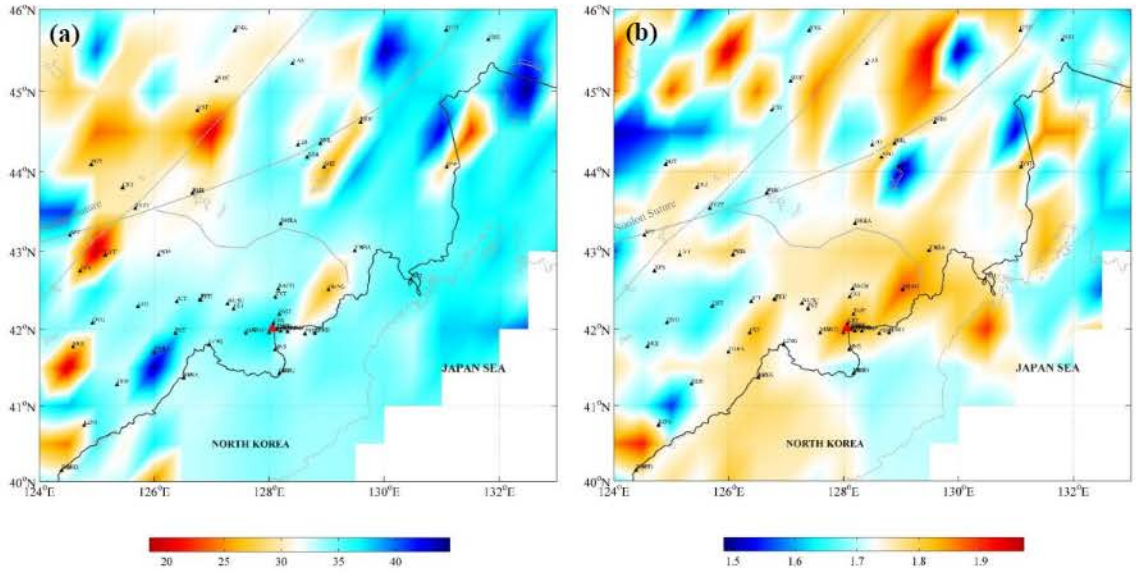

Figure 5. 2D relief maps for crustal thickness **(a)** and average crustal Vp/Vs ratio **(b)** around the CBS volcanic area derived from the results of H-κ analysis on receiver function data. The 2D maps are interpolated from station measurements using the ordinary kriging method.

The increased crustal thickness and Vp/Vs ratio show that a large region of the crust around the CBS volcano has been modified by magmatism associated with the volcanism. These features indicate an upwelling channel of the asthenospheric material with a high mafic composition, and the mafic intrusion attaches to the bottom of the crust and thus deepens the Moho beneath the volcano. However, a high mafic composition is not sufficient to explain Vp/Vs ratios higher than 1.87. Such high values of Vp/Vs suggest that partial melt is present in the crust beneath the CBS. This region of melt represents a potential source for magmas erupted in the last few thousand years and may be associated with an episode of volcanic unrest observed between 2002 and 2005, but the crustal average Vp/Vs ratios cannot either explicitly identify the potential magma reservoir/chamber in the crust or determine the location and size of the magma reservoir.

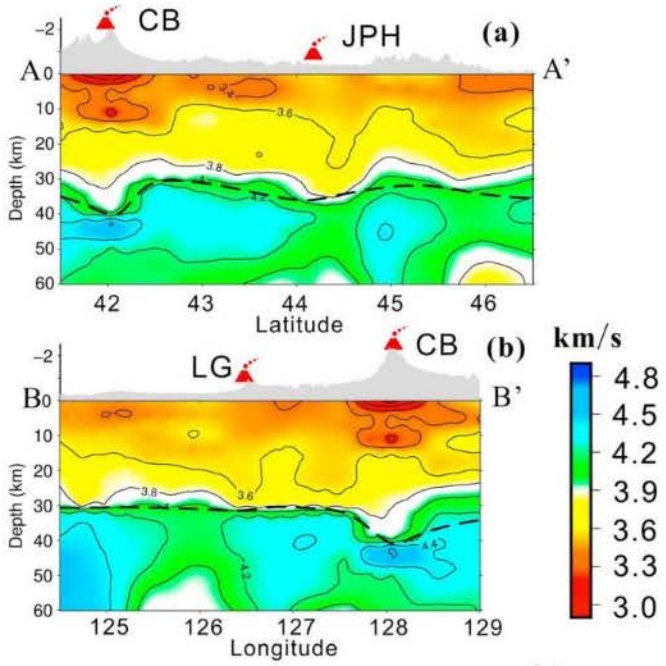

Figure 6. Vertical cross-sections of S wave velocity tomography across the CBS. The red triangles denote volcanoes. The black dash line denotes the Moho discontinuity estimated from the receiver-function stacking. This figure is taken from Figure 11 in Zhu et al. [2019].

Hetland et al. [2004] resolved a low-velocity anomaly extending from about 5–10 to 15–25 km below the surface, indicating a region of elevated temperatures. However, they were unable to determine if partial melt is presented based on the data used in their study. Wu et al. [2009] inverted for a 1D S-wave velocity model using the receiver functions on a station near the CBS crater. Their model showed a low-velocity layer at 8km extending to 28km with the lowest S-wave velocity of ~2.2 km/s. Such a low velocity indicates the existence of the high-temperature material or magma reservoir in the crust beneath the CBS crater. While at a station located 50km north of the crater, no obvious crustal low-velocity layer was detected in Wu et al. [2009], suggesting the magma reservoir extends less than 50km laterally. The common conversion point migrations performed by Hammond et al. [2020] on the receiver function data recorded at deployment 1U also detected a low-velocity zone extending ~30km deep from the volcano summit. This low-velocity zone corresponds to a melt-rich region with the top found 4-8km below sea level, with the shallowest depth directly beneath the volcano. The base to this melt-rich region could not well be constrained, suggesting melt is pervasive throughout the crust. On the other hand, the low-velocity zone determined by a joint inversion of surface wave and receiver functions extended to ~100km in the north and south directions from the CBS volcano laterally [Zhu et al., 2019]. Although the depth of the low-velocity zone beneath the volcano determined by Zhu et al. [2019] is 8 – 15 km (Figure 6), similar to that determined by Hetland et al. [2004] and Hammond et al. [2019], the lateral extent revealed by Zhu et al. [2019] is much wider than the results of the other two studies, implying a larger magma reservoir in the mid crust. The joint inversion of surface wave and receiver functions performed by Chen and Niu [2016] on the permanent stations also revealed low-velocity zones in the mid-crust and lower-crust beneath the CBS volcano (Figure 7), however, the S-velocity value of low-velocity zone is not as low as that resolved in Zhu et al. [2019].

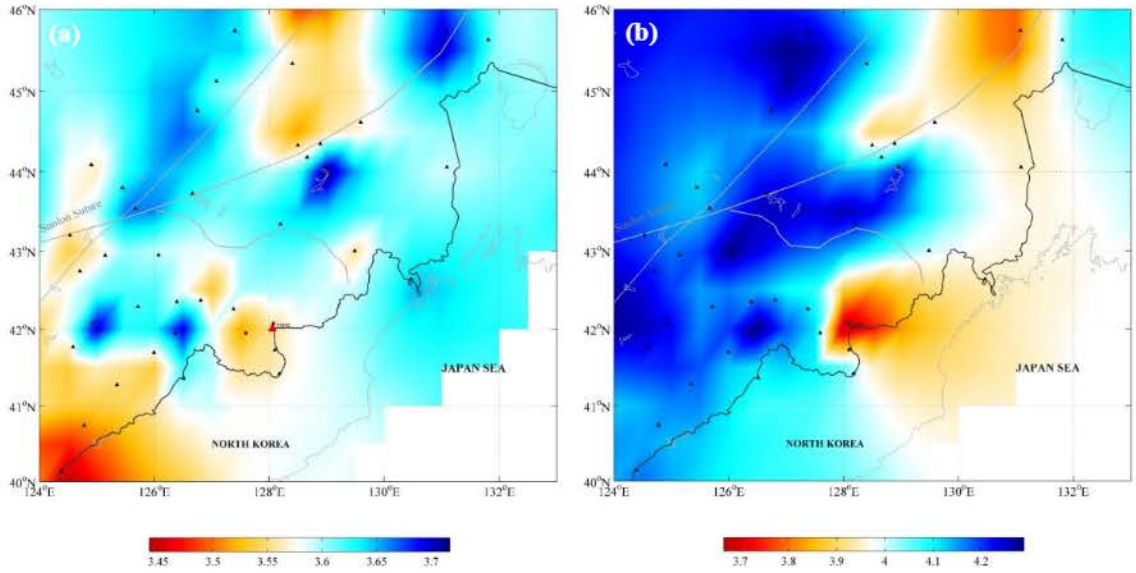

Figure 7. 2D relief maps for S-velocities at **(a)** 14km and **(b)** 35km. The S-velocities of individual stations are taken from the joint inversion of surface wave and receiver functions performed by Chen and Niu [2016]. The 2D maps are interpolated from station measurements using the ordinary kriging method.

1.3 Purposes of This Study

These reviewed studies all revealed thickened crust, high bulk crustal Vp/Vs ratio, and low-velocity zone in the mid-crust beneath the CBS volcano, suggesting partial melt in the mid-crust beneath the volcano. The partial melt is very likely related to a magma reservoir in the mid-crust. These results support the "big mantle wedge" model that the CBS volcanisms are caused by hot and wet mantle upwelling associated with subduction driven corner flow in the big mantle wedge above the stagnant Pacific slab in the mantle transition zone. Due to the resolving capability of the seismic techniques and data used in these studies, considerable discrepancies are found in their results. For example, the inherent trade-off between H and κ in the H-κ analysis may yield two pairs of H and κ, one with a higher H value and lower κ value and the other with lower H value and higher κ value. In a region with complex crustal structures, special inspection combining geological knowledge is required to identify the appropriate results [Ri et al., 2016]. Moreover, as the average crustal Vp is a free parameter in H-κ analysis, choosing different Vp values will also affect the results.

Because each station has its own velocity model, the ideal method is to perform 3D ray tracing to determine the location and size of the magma reservoir. Since many deep-focus earthquakes occurred within the Wadati-Benioff seismic zone of the subducting Pacific slab, the seismic rays of these deep earthquakes to the stations in NE China will fully scan the areas underneath CBS volcano. It thus provides us an opportunity to study the CBS volcano using ray tracing method. The purpose of this study is to perform comprehensive ray tracing of deep earthquakes to detect the magma reservoir beneath the CBS volcano, determining its location, size, and degree of melt. Those previous studies provide valuable knowledge to help us construct 1D and 3D velocity models and choose parameters required by the ray tracing method.

2 SEISMIC DATA

Many temporal seismic stations have been deployed around the CBS volcanic region to study this volcano. The temporal seismic stations selected for this study include 1U (Mt. Paektu Seismic Network), XI (Study of Changbai Volcanoes and Deep Subduction Zone), XL (North Korea Nuclear Site Investigation), and YP (Northeast China Extended Seismic Array), and one deployment belonging to Chinarray (network code V0; Figure 8). These temporal stations were usually operated from several months to several years. They may not be able to capture sufficient seismic events satisfying our requirements. For example, the open information from Chinarray claimed that the operation period of V0 was from 2006 to 2008, but our Chinese collaborators verified that network V0 had only been deployed on the CBS for about six months in 2006 and then was moved to other areas. This makes us obtain the seismograms of only four deep earthquakes (Table 1). For this reason, we also select permanent stations in NE China: HL (Heilongjiang province), JL (Jilin province), and LN (Liaoning province) (Figure 8). Each of these three regional seismic networks consists of ~50 stations that have been updated from analog stations or established since 2009. These regional seismic networks are part of the Chinse National Digital Seismic Network (CNDSN) and their waveform data are archived in the Chinese Earthquake Network Center (CENC). We downloaded the waveform data of PASSCAL-type seismic deployments from IRIS-DMC. We retrieved the waveform data of CNDSN and V0 from CENC and the Institute of Geophysics, CEA, respectively, through the collaboration program between ARRAY and Chinese collaborators.

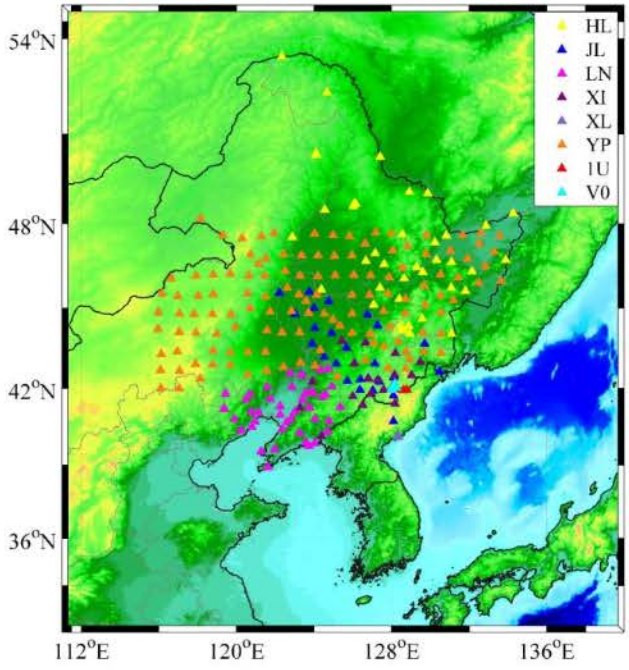

Figure 8. Distribution of seismic stations used in this study.

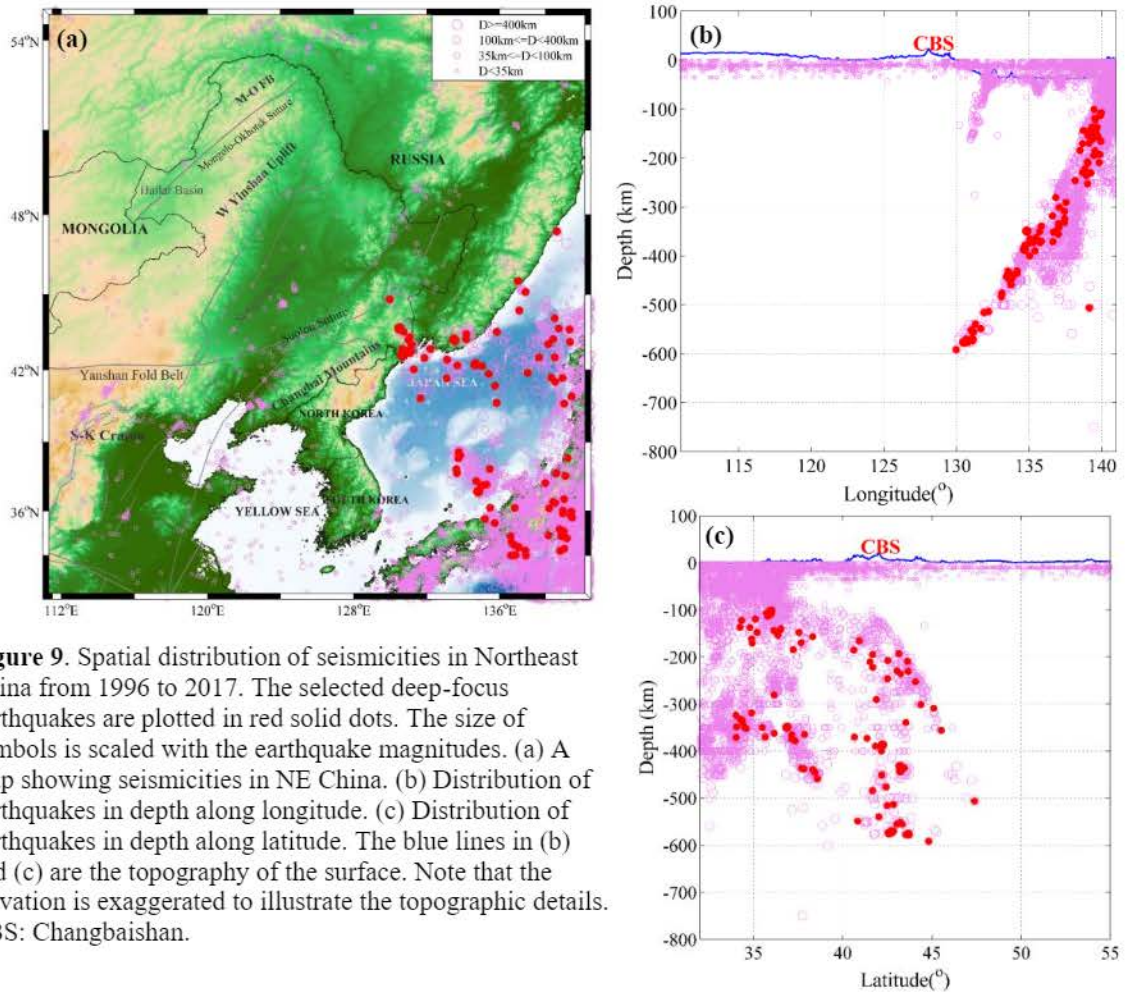

Figure 9. Spatial distribution of seismicities in Northeast China from 1996 to 2017. The selected deep-focus earthquakes are plotted in red solid dots. The size of symbols is scaled with the earthquake magnitudes. (a) A map showing seismicities in NE China. (b) Distribution of earthquakes in depth along longitude. (c) Distribution of earthquakes in depth along latitude. The blue lines in (b) and (c) are the topography of the surface. Note that the elevation is exaggerated to illustrate the topographic details. CBS: Changbaishan.

From NE China to Japan Trench is an area with a relatively high seismicity rate, including a large number of shallow-focus earthquakes that occurred within the crust (depth < ~35km) and deep-focus earthquakes that occurred at depths of 100 – 600km (Figure 8). The grouped activities of shallow-focus and deep-focus earthquakes in NE China more or less are related to the collision between the west Pacific plate and the Eurasian plate, as well as the form of the subduction of the Pacific plate [e.g., Sun and He, 2004; Zhu et al., 2010]. The deep-focus earthquakes all occur within the Wadati-Benioff seismic zone of the subducting Pacific slab beneath the Japan Sea and the northeastern Eurasian continent margin.

These deep-focus earthquakes are good seismic sources to detect the magma reservoir beneath the CBS volcano by performing ray tracing in that the seismic rays of these deep earthquakes propagate directly through the media beneath the CBS to arrive at the stations on the surface. If there exists a magma reservoir beneath the CBS volcano, the S-wave shadows and P-wave delays are expected to be observed on these densely deployed seismic stations when the seismic rays traverse the magma reservoir. The physical properties of the magma reservoir can then be investigated using these seismic data.

According to the availability of waveform data on our selected stations, our selections for deep earthquakes near the CBS volcanic region focus on years from 1996 to 2017. Along with the subducting direction of the Pacific slab, earthquakes at ~100km deep occur in the Japan Sea, about

1000km far from the CBS area horizontally. The earthquakes at 410 – 660km deep are located directly beneath the CBS volcano, concentrating on the stagnant Pacific slab in the mantle transition zone. Because the deep earthquakes that occurred at various depths propagate along different paths to arrive at the same stations, the behaviors of observed P- and S-wave will help to constrain the location and range of the magma reservoir. Among the earthquakes shown in Figure 9, we finally select 73 deep-focus earthquakes with a minimum magnitude of 4.5 (red solid circles in Figure 9). The source information of these selected events is summarized in Table 1. We have tried to make use of even smaller earthquakes, but these small earthquakes are hardly be captured by the used stations with clear waveforms given the long travel distances. The waveform data that are selected for this study must be recorded by at least four stations. The redundancy of selected earthquakes ensures sufficient seismic data for our study.

Table 1: Source Information of Selected Deep-focus Earthquakes

Origin time	Lat (°)	Lon (°)	Depth (km)	Mag	Event ID	Recording Networks
1996- 1-30 21 14 56.52	36.1478	135.4776	362.3	4.87 mb	1996.01.30_21.14.565	XL
1996- 7-24 0 50 14.45	34.2366	137.4116	332.0	4.64 mb	1996.07.24_00.50.145	XL
1996-10-30 9 9 41.79	41.6837	138.8225	222.0	5.26 mb	1996.10.30_09.09.418	XL
1996-11-25 0 26 38.50	38.4323	133.8347	444.8	4.56 mb	1996.11.25_00.26.385	XL
1996-12- 3 15 49 14.33	37.5435	139.5868	147.9	5.20 mb	1996.12.03_15.49.143	XL
1996-12-22 14 53 29.25	43.2387	138.9306	235.5	5.97 mb	1996.12.22_14.53.293	XL
1998- 6-16 20 10 0.95	34.7933	139.6700	137.2	4.68 mb	1998.06.16_20.10.010	XI
1998- 8-20 9 36 35.75	45.5208	136.9960	355.8	5.22 mb	1998.08.20_09.36.358	XI
1999- 4- 8 13 10 35.60	43.6690	130.5061	576.5	6.39 mb	1999.04.08_13.10.356	XI
1999- 4-18 23 14 20.20	34.3236	139.5332	122.4	4.84 mb	1999.04.18_23.14.202	XI
1999- 8- 8 21 39 38.80	35.8046	139.8837	113.6	4.70 mb	1999.08.08_21.39.388	XI
1999-10- 1 3 47 22.93	37.6635	139.1043	170.0	4.52 mb	1999.10.01_03.47.229	XI
1999-10- 3 4 6 46.08	35.6520	135.1809	370.0	4.58 mb	1999.10.03_04.06.461	XI
1999-12- 5 7 28 33.21	42.5143	139.0081	207.8	4.80 mb	1999.12.05_07.28.332	XI
1999-12-31 13 9 12.98	37.3216	134.7162	378.3	5.04 mb	1999.12.31_13.09.130	XI
2006- 2- 1 11 35 53.75	35.7145	139.9657	107.1	4.79 mb	2006.02.01_11.35.538	V0
2006- 4-24 4 28 14.93	38.3111	139.7299	156.4	4.71 mb	2006.04.24_04.28.149	V0
2006- 5-10 16 47 50.79	43.6323	139.8185	209.3	4.89 mb	2006.05.10_16.47.508	V0
2006- 9-16 2 22 50.96	41.3524	135.7497	373.0	5.12 mb	2006.09.16_02.22.510	V0
2006-11-27 19 26 5.70	37.6686	133.6624	436.2	4.70 mb	2006.11.27_19.26.057	V0
2009- 1-22 0 9 34.34	40.9160	139.9378	165.6	4.73 mb	2009.01.22_00.09.343	YP
2009- 1-22 12 21 0.71	34.2208	139.3105	137.0	4.73 mb	2009.01.22_12.21.007	YP
2009- 1-26 8 54 21.87	36.5283	139.5196	139.7	4.51 mb	2009.01.26_08.54.219	YP
2009- 3-13 9 7 1.93	43.2398	134.1631	430.5	4.83 mb	2009.03.13_09.07.019	YP
2009- 4-18 3 56 31.38	42.8457	130.6792	569.5	4.77 mb	2009.04.18_03.56.314	YP
2009- 6-10 4 7 2.73	34.5810	136.6598	351.6	4.53 mb	2009.06.10_04.07.027	YP
2009- 7-16 6 29 4.44	42.4150	133.1157	476.1	4.91 mb	2009.07.16_06.29.044	YP
2009- 8-10 12 42 53.15	43.5266	130.7373	577.1	4.81 mb	2009.08.10_12.42.532	YP
2009-11-15 20 31 34.56	44.3784	137.0688	301.1	4.69 mb	2009.11.15_20.31.346	YP
2009-12-24 0 23 32.25	42.1656	135.0247	400.0	5.12 mb	2009.12.24_00.23.323	YP
2009-12-24 0 23 33.38	42.2277	134.6670	386.8	6.02 mb	2009.12.24_00.23.334	YP; HL; JL: LN
2010- 2- 5 6 48 10.25	40.6537	135.8279	370.1	4.93 mb	2010.02.05_06.48.103	YP;
2010- 2-18 1 13 18.35	42.5934	130.6807	573.9	6.16 mb	2010.02.18_01.13.184	YP; HL; JL; LN
2010- 4-29 15 19 9.66	37.1389	135.0504	365.1	4.60 mb	2010.04.29_15.19.097	YP;
2010- 8-26 15 8 4.94	36.1401	136.8238	280.7	5.09 mb	2010.08.26_15.08.049	YP;
2010- 9-21 20 15 10.08	40.6143	139.5297	185.2	4.66 mb	2010.09.21_20.15.101	YP;

2011- 1- 7 23 34 10.64	43.0290	131.1629	555.3	4.77 mb	2011.01.07_23.34.106	YP; HL; JL; LN
2011- 5-10 15 26 5.05	43.3199	131.0913	554.9	5.34 mb	2011.05.10_15.26.051	YP; HL; JL; LN
2011-12-14 7 48 44.48	42.5060	138.1551	245.8	4.64 mb	2011.12.14_07.48.445	YP;
2013- 4- 5 13 0 2.36	42.7359	131.0640	571.3	6.16 mb	2013.04.05_13.00.024	HL; JL; LN
2013- 4- 6 0 29 55.51	42.7356	131.0457	572.3	5.38 mb	2013.04.06_00.29.555	HL; JL; LN
2013- 4-14 1 22 4.51	36.0253	139.4564	100.7	4.66 mb	2013.04.14_01.22.045	HL; JL; LN
2013- 9- 2 2 51 13.21	42.1874	133.6783	450.5	5.46 mb	2013.09.02_02.51.132	1U
2013- 9-11 7 11 31.98	43.1307	139.8445	192.9	4.83 mb	2013.09.11_07.11.320	1U
2013- 9-27 18 36 41.39	43.4515	134.1685	435.3	4.67 mb	2013.09.27_18.36.414	1U
2013- 9-30 0 11 54.90	43.0402	138.6556	229.2	4.71 mb	2013.09.30_00.11.549	1U
2013-10-29 20 17 50.09	43.2148	131.0068	551.2	4.97 mb	2013.10.29_20.17.501	1U
2013-11-12 11 36 3.89	41.6686	139.4386	194.7	4.64 mb	2013.11.12_11.36.039	1U
2013-11-18 19 10 45.72	34.3653	137.0281	334.2	5.24 mb	2013.11.18_19.10.457	1U
2014- 1- 1 7 4 4.31	41.8791	137.5303	290.5	4.85 mb	2014.01.01_07.04.043	HL; JL; LN
2014- 1-11 3 56 48.46	43.6640	139.2354	230.4	5.04 mb	2014.01.11_03.56.485	HL; JL; LN
2014- 2-20 1 32 51.73	42.8482	132.1958	513.4	4.53 mb	2014.02.20_01.32.517	HL; JL; LN
2014- 5- 4 20 18 25.01	34.8781	139.3660	161.4	5.76 mb	2014.05.04_20.18.250	HL; JL; LN
2014- 5-15 9 48 13.46	35.0993	139.5026	119.1	4.53 mb	2014.05.15_09.48.135	HL; JL; LN
2014- 6-28 5 51 5.60	36.3617	139.0394	153.8	4.51 mb	2014.06.28_05.51.056	HL; JL; LN
2014-12- 5 16 1 56.43	35.4731	135.7285	350.1	4.61 mb	2014.12.05_16.01.564	HL; JL; LN
2015- 1-19 22 34 48.98	37.2277	138.4885	184.7	4.80 mb	2015.01.19_22.34.490	HL; JL; LN
2015- 2- 7 16 40 5.27	43.5318	135.8359	339.2	4.58 mb	2015.02.07_16.40.053	HL; JL; LN
2015- 4-12 6 25 14.67	36.4120	138.9224	145.7	4.53 mb	2015.04.12_06.25.147	HL; JL; LN
2015- 5- 3 14 30 15.92	36.1261	138.7045	143.9	4.81 mb	2015.05.03_14.30.159	HL; JL; LN
2015- 5-25 6 37 40.72	41.8428	135.4000	389.7	4.87 mb	2015.05.25_06.37.407	HL; JL; LN
2015-11- 7 13 44 44.50	35.9826	139.9191	108.7	5.09 mb	2015.11.07_13.44.445	HL; JL; LN
2016- 1- 2 4 22 19.26	44.8106	129.9676	591.3	5.70 mb	2016.01.02_04.22.193	HL; JL; LN
2016- 1-18 0 56 46.92	35.1955	139.2737	147.6	4.57 mb	2016.01.18_00.56.469	HL; JL; LN
2016- 7-17 9 43 24.78	34.4010	137.0381	342.0	4.68 mb	2016.07.17_09.43.248	HL; JL; LN
2016-11-11 4 53 37.44	34.4864	136.7937	349.7	4.65 mb	2016.11.11_04.53.374	HL; JL; LN
2017- 1-12 17 4 57.77	41.6636	133.0924	483.7	5.03 mb	2017.01.12_17.04.578	HL; JL; LN
2017- 2-15 19 41 0.63	37.1673	135.2676	372.7	4.57 mb	2017.02.15_19.41.006	HL; JL; LN
2017- 3-20 8 22 28.04	44.0705	139.0117	252.6	4.50 mb	2017.03.20_08.22.280	HL; JL; LN
2017- 4-12 7 34 59.47	38.5718	133.7558	458.9	4.57 mb	2017.04.12_07.34.595	HL; JL; LN
2017- 6-13 23 37 33.11	37.1301	134.9809	374.0	4.51 mb	2017.06.13_23.37.331	HL; JL; LN
2017- 7-12 19 48 7.37	40.8368	131.6599	548.7	5.87 mb	2017.07.12_19.48.074	HL; JL; LN
2017-11-30 9 18 23.60	38.3084	133.7282	438.9	5.18 mb	2017.11.30_09.18.236	HL; JL; LN

3 P-WAVE DELAYS AND S-WAVE SHADOWS

3.1 Picking P- and S-wave Arrivals

We manually pick P- and S-arrivals on each seismogram of the selected earthquakes. This is a critical step in this study because the actual P- and S-wave travel time will be compared to the predicted travel time to determine the velocity model beneath the CBS volcano through the error-and-trial or more sophisticated inverse method. Initially, we use two types of 1D crustal and upper mantle velocity models to predicted P- and S-arrivals. The first model is AK135 global model [Kennett et al. 1995] and the second model is a regional model for NE China (Figure 10). Chen and Niu [2016] obtained 1D velocity models beneath ~1000 CNDSN stations across China by joint inversion of receiver function and surface wave dispersion data. The NE China model used here is the average of selected 1D models of NE China stations. As the receiver function and surface wave data used by Chen and Niu [2016] have little sensitivities for the upper mantle deeper than 150km,

we use the AK135 model for the mantle deeper than 150km. The upper mantle in the NE China model generally has lower Vs and Vp than the global average. The Moho depth in NE China is determined in the range of ~32 - ~35km using the receiver function data of individual stations, but it is smoothed as a transition zone in the model (Figure 10) when we average many individual station velocity profiles. Compared to the AK135 model, the NE China model displays a low-velocity zone in the lower crust.

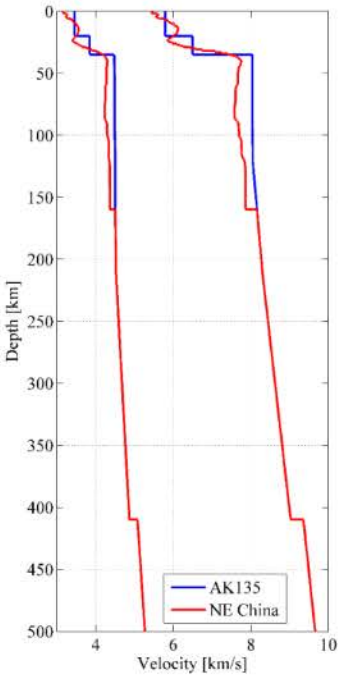

Figure 10. Vp and Vs models used to predict the arrivals of P and S phases. The blue lines are the global AK135 crustal and upper mantle models. The red lines are the regional models for NE China, which are averages of individual 1D models on the stations in NE China.

Figure 11 shows the three-component seismograms of event 2010.02.18_01.13.184 (Table 1) recorded at JL.BST, a station located ~200km from the CBS crater. On each component, the S-wave is either missed (Z-component) or weaker than the P-wave (E-component). The S-wave amplitude on N-component is clear, but the energy mostly concentrates in low frequencies. The green and magenta bars in Figure 11 indicate the predicted P- and S-arrivals, respectively, calculated using the NE China regional models. The P-wave arrives later than the predicted arrival time.

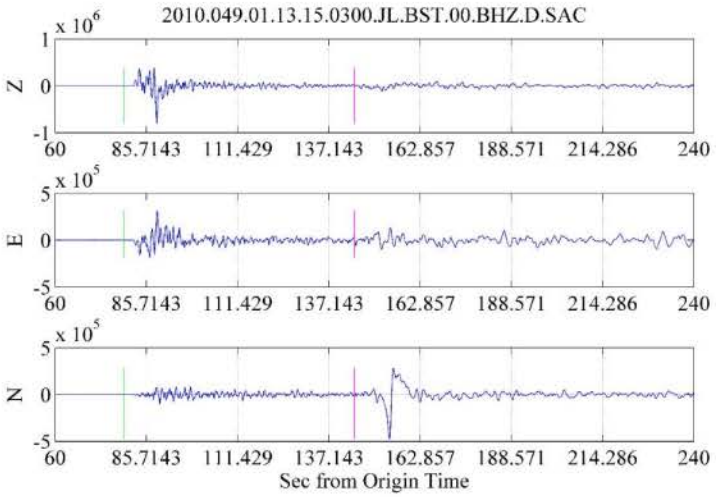

Figure 11. 3-components seismogram of a deep earthquake occurred on 2010-2-18, 1:13:18.35 recorded by JL.BST. The green and magenta bars indicate the predicted P- and S-arrivals, respectively, calculated using the NE China regional models.

With reviewing more seismograms in the phase-picking process, more typical seismograms with P-wave delays and S-wave shadows have been found. Figure 12 shows the seismograms of another deep earthquake 2011.01.07_23.34.106 (Table 1) recorded at JL.CBS and LN.SNY. JL.CBS is a station located on CBS Mountain. The S-waves are unidentifiable on all three components of the seismogram recorded at this station. In contrast, the station LN.SNY (near Shenyang City in Liaoning province) is far from the CBS volcano area, and the S-wave on the seismogram of this station is clear with amplitudes stronger than the P-wave amplitudes (Figure 12b).

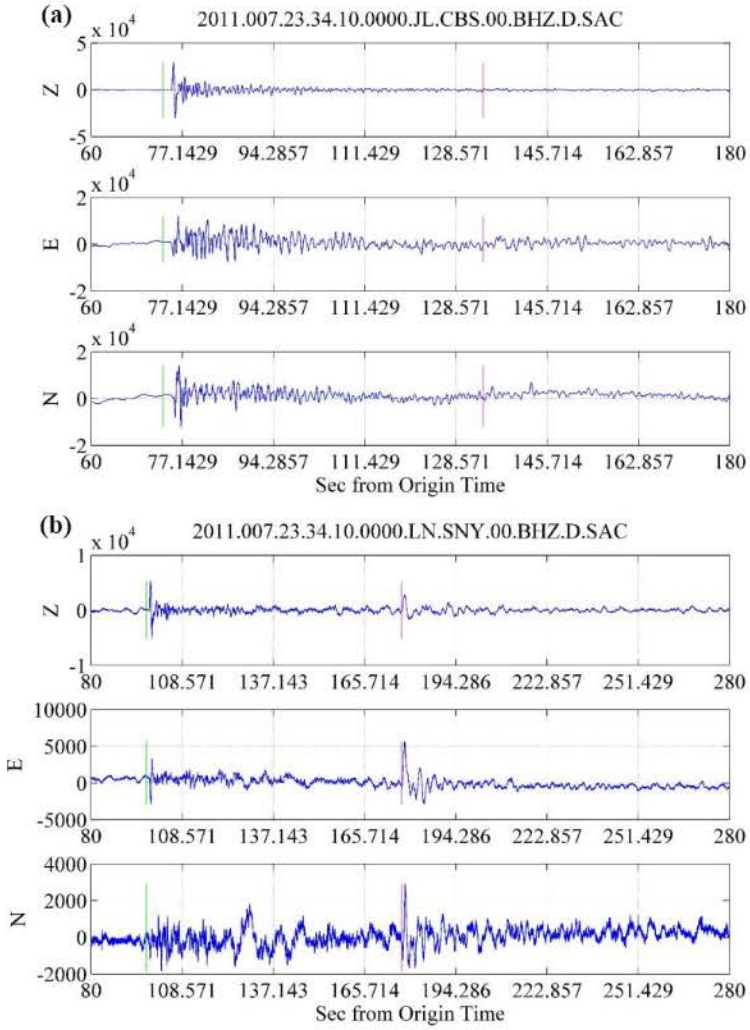

Figure 12. 3-components seismogram of a deep earthquake occurred at 2011-1-7, 23:34:10.64 recorded at (a) JL.CBS and (b) LN.SNY. The green and magenta bars indicate the predicted P- and S- arrivals, respectively, calculated using the NE China regional models.

3.2 Observation of P-wave Delays

During the procedure of data processing, we observe P-wave delays and S-wave shadows when the seismic rays of a deep earthquake propagate through the media below the CBS areas. Figures 13 and 14 show the vertical-components seismograms that were recorded at the stations along two separate paths for the earthquake 2011.05.10_15.26.051 (Table 1). One path is at azimuth = 240°, crossing through the CBS volcanic region. On all stations along this path, we observe clear P-wave delays (Figure 13a). Meanwhile, S-waves are missing at four stations near the CBS volcano but appear on the stations far away from the CBS volcano. Keep in mind that this earthquake is 554.9km deep (Table 1) so that the travel paths plotted on the map (Figure 13b) are the surface projections of the actual travel paths. The reason that S-wave shadows appear only at near-field stations but not at far-field stations is probably that the partial-melt magma reservoir is limited in a small region right below the CBS volcano so that those seismic rays recorded at far-field stations do not propagate through the magma reservoir. It is also possible that the magma reservoir extends to a large area but the parts at the edge are not so weak as to prevent the propagation of S-waves.

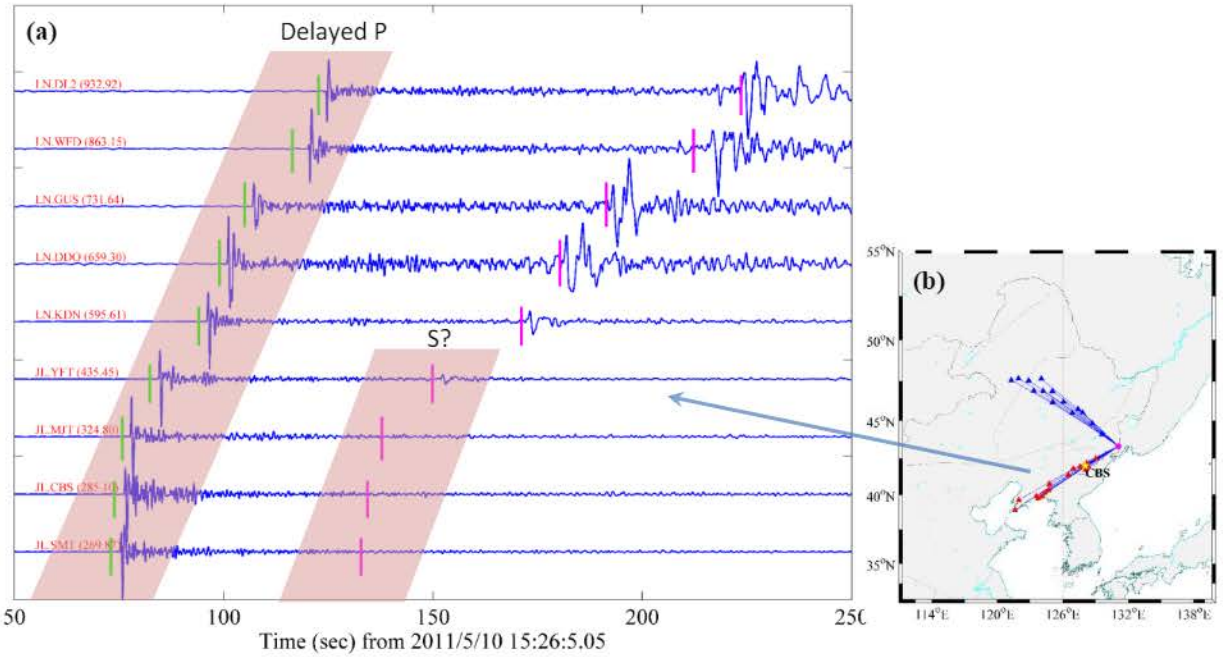

Figure 13. (a) Vertical-component seismograms of a deep earthquake 2011.05.10_15.26.051. These seismograms are recorded on the paths that the seismic rays of the earthquake propagate through the CBS regions. The seismograms are aligned in the order of their epicentral distances. The green and magenta bars on each seismogram denote predicted P and S arrivals, respectively. (b) Inserted map showing seismic rays propagating along two separate paths. One path is at azimuth = 240°, crossing CBS regions, and the other is at azimuth = 310°, away from CBS regions.

Figures 14 shows the vertical-components seismograms of this earthquake that are recorded at the stations on the path with azimuth = 310°. This path is away from the CBS areas. In contrast to Figure 13, we do not observe P-wave delays on all stations along this path. The S-waves on some stations are weak, suggesting the CBS magma reservoir extends northwards to a large area. However, using only one earthquake cannot completely explain our observations. We cannot determine the location and range of the CBS magma reservoir until we compute more seismic rays that fully scan the media below the CBS volcanic region.

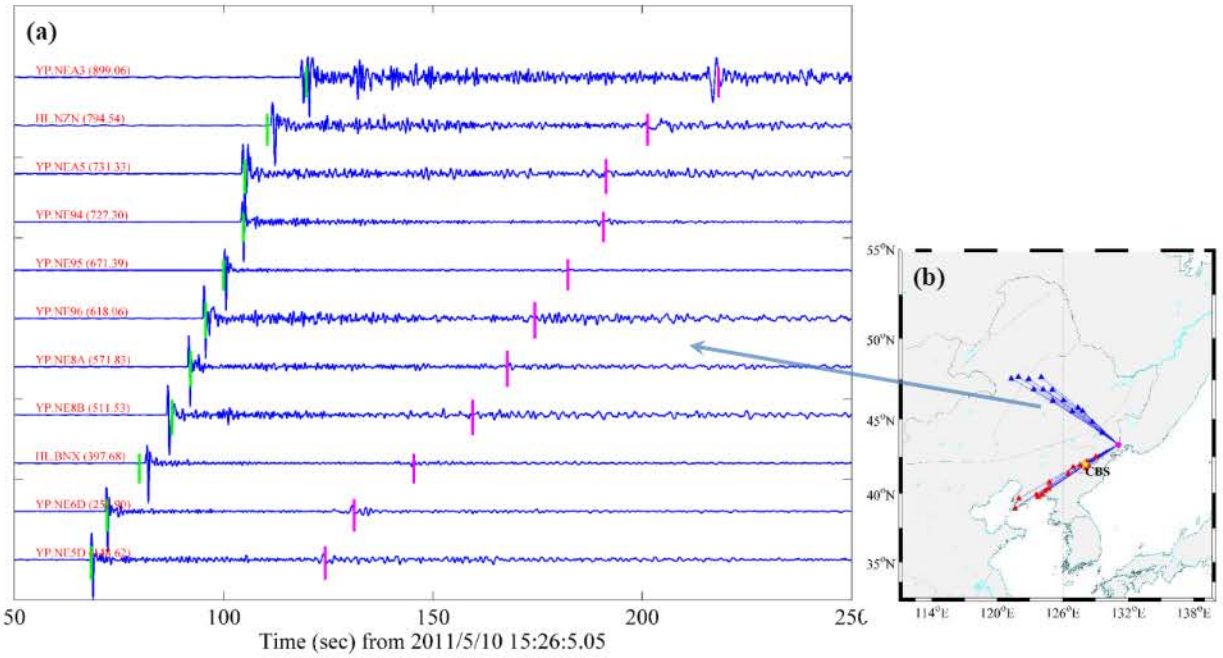

Figure 14. Same as Figure 13, but for seismograms of the deep earthquake propagating to a direction at azimuth = 310°.

3.3 Classification of S-wave Shadows by S/P Ratios

Missing and weak S-waves mean that seismic waves must propagate through a block that is so hot or half molten that prevents the propagation of S-wave. If such a hot block is the magma reservoir either in the crust or in the upper mantle beneath the CBS volcano, the phenomena of Missing and weak S-waves will show a positive correlation with the spatial distribution of the stations receiving S-waves: missing and weak S-waves shall be observed at the stations near the CBS volcanic region, whereas clear S-waves are observed at far stations from the volcano.

To quantify S-wave shadows, we calculate the ratio of S-wave amplitudes to P-wave amplitudes on each station. Using the picked P arrival as the starting point, we set a 5s window as the direct P wave duration and calculate P-wave RMS amplitude. Similarly, the S-wave RMS amplitude is calculated using picked S arrival and a 10s window. If the S arrival is unidentifiable, the calculated S arrival using the NE China model is used. The S/P amplitude ratio is then calculated as an indicator of S-wave shadows for a station. Figure 15a shows the spatial distribution of stations with calculated S/P amplitude ratios for event 2010.02.18_01.13.184 (Table 1). The values of S/P ratios are shown by the colors plotting station symbols, with red for the minimum S/P value and blue for the maximum S/P value. Similarly, Figure 15b shows the distribution of S/P amplitude ratios for another event 2011.01.07_23.34.106 (Table 1).

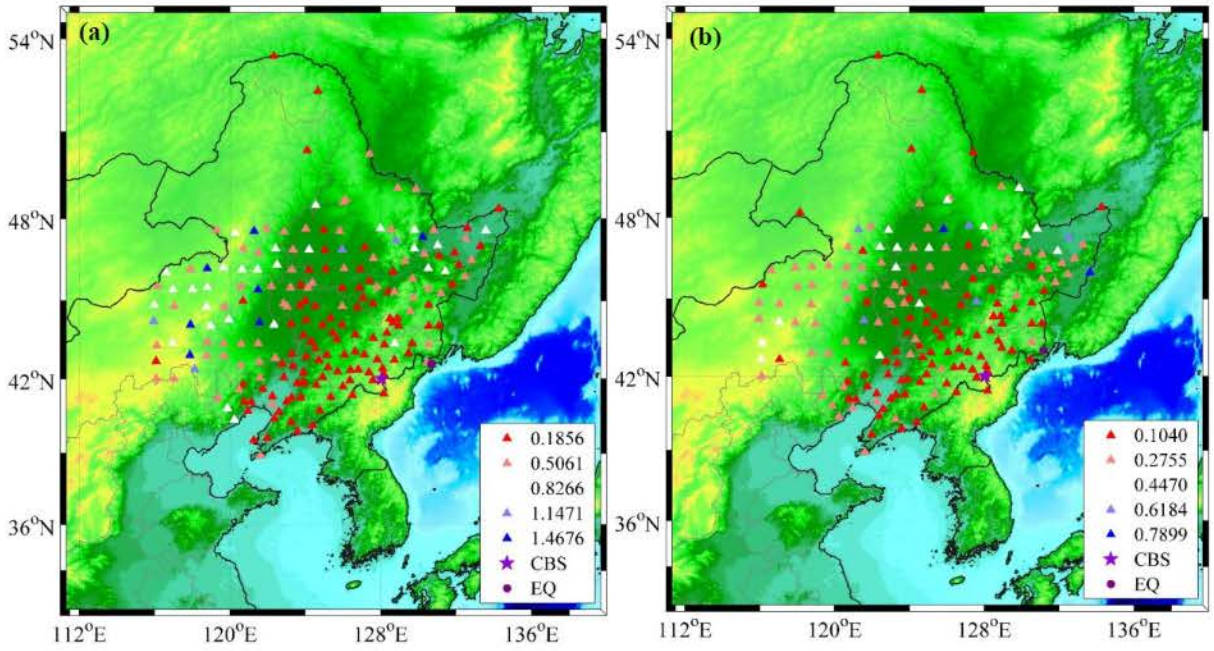

Figure 15. Spatial distribution of surface stations with S/P amplitude ratios for (a) the deep earthquake that occurred at 2010-2-18, 1:13:18.35 and (b) the deep earthquake occurred at 2011-1-7, 23:34:10.64. The triangles stand for stations and the colors of triangles indicate the values of S/P amplitude ratios. The purple star indicates the CBS volcano.

The spatial distribution of S/P ratios delimits an approximate range of the CBS magma reservoir mapping on the free surface. Most stations in the red color concentrate around the CBS volcanic region and extend northwards to NE China. As the seismic rays of the deep earthquake arrive at these stations at a nearly vertical incidence angle, the magma reservoir prevents S-wave from propagating to the stations through the reservoir. If the magma reservoir is located at the mid-crust, it very likely extends to a broader region so that the S-wave propagation to further stations is also affected. If it is located at the upper mantle, however, a limit-sized magma reservoir can also affect the S-wave propagation to the stations far away from the reservoir.

To determine the size and depth of the magma reservoir, we need to make use of more deep earthquakes with different incidence angles but recorded at the same stations. These earthquakes scan different parts of the crust and upper mantle below the CBS volcano. Examining the behaviors of P-wave delays and S-wave shadows will determine the size and depth of the magma reservoir [e.g, Lin, 2016; Lin et al., 2018].

4 SEISMIC RAY TRACING

4.1 Complete Ray Tracing Method

Ray tracing consists of the computation of a ray, i.e., in a step-by-step evaluation of coordinates of points along the ray. The seismic ray in 3D structures can be expressed as the following second-order ordinary differential equation (ODE) governing the ray path.

$$\frac{d}{ds}\left(\frac{1}{v}\frac{dr}{ds}\right) = \nabla\left(\frac{1}{v}\right) \quad (1)$$

where $\boldsymbol{r}$ is the spatial position vector and s is an independent variable representing the path length along the ray. The term $d\boldsymbol{r} = dx^i$, $i = 1, 2, 3$ and $\frac{d\boldsymbol{r}}{ds}$ is the tangent vector. The velocity $v(\boldsymbol{r})$ is also a function of the spatial position vector $\boldsymbol{r}$. This second-order ODE system can be reduced to a system of first-order ODEs by defining the slowness vector $\mathbf{p}(s) = \frac{1}{v}\frac{d\boldsymbol{r}}{ds}$. Then Equation (1) can be rewritten as:

$$\frac{d\boldsymbol{r}}{ds} = v\mathbf{p}, \ \frac{d\mathbf{p}}{ds} = \nabla\left(\frac{1}{v}\right) \tag{2}$$

with six components:

$$\frac{dx^i}{ds} = vG^{ij}p_j, \frac{dp_i}{ds} = -v^{-2}\frac{\partial v}{\partial x^i} + v\Gamma_{ij}^k G^{jl}p_k p_l \tag{3}$$

where $G^{ij} = G^{ij}(x^k)$, $i, j, k = 1, 2, 3$, is the contravariant components of the metric tensor describing different coordinate systems, and Γ_{ij}^k is the Christoffel symbols, which are the combination of covariant components $G_{ij} = G_{ij}(x^k)$ and contravariant components $G^{ij} = G^{ij}(x^k)$ of the metric tensor:

$$\Gamma_{ij}^k = \frac{1}{2}G^{kl}\left(G_{il,j} + G_{jl,i} - G_{ij,l}\right) \tag{4}$$

To keep track of the travel time $t(s)$ we may add a seventh equation:

$$\frac{dt}{ds} = \frac{1}{v} \tag{5}$$

The integral of Equation (5) yields the real-valued travel time.

In this study, we implement ray tracing simulations using the complete ray tracing (CRT) method developed in Červeny and Klimeš [1984] and Červeny et al. [1988]. In contrast to the standard ray tracing in which only the ray trajectory, travel times, and slowness vectors along the ray are determined, the CRT method consists of (a) computation of ray tracing and travel time along the ray (standard ray tracing), (b) determination of the polarization vectors along the ray, (c) dynamic ray tracing through the computation of the ray propagator matrix and (d) evaluation of the components of the reduced vectorial complex-valued amplitudes.

The output of the CRT program includes basic quantities along a ray, such as trave time, imaginary part of the complex-valued travel time (t^*), coordinates of points along the ray, covariant components of the slowness vector, covariant components of the polarization vector, ray propagator matrix, and complex-valued vectorial reduced amplitudes, and many auxiliary quantities. Not only the quantities along each seismic ray, the quantities at the interface between nearby blocks are also output for various seismological applications. At an interface, the ray is transformed following the Snell law. The CRT program is thus a powerful tool with many important seismological applications. Using the various quantities along the ray and at intersections of the ray with some selected surfaces, the CRT can be used as a basic procedure in many program packages in the numerical modeling and interpretation of high-frequency seismic wavefields in complex 3D structures with laterally varying layered and blocked structure [Červeny et al., 1988]. For example, the CRT can deal with ray amplitudes and paraxial ray approximation for ray amplitudes, to generate synthetic body-wave seismograms.

4.2 Model Construction for CRT Program

The parameters used to describe the 3D model and seismic rays and to control the ray tracing computation are organized in multiple input files. The most complicated input file is the one to describe a 3D model. The model is implemented using descriptive ways, i.e., the model is defined inside a volume of space by smooth functions specifying the distribution of the parameters of the medium. The parameters include interfaces and blocks and the velocities and attenuation of blocks. "Smooth" means that the parameters and their first and second partial derivatives must be continuous. Because the model may contain blocks with sharp edges where their first and second partial derivatives do not exist, the algorithm uses a special method to construct the model using two types of blocks formed by smooth surfaces: simple blocks (SBs) and complex blocks (CBs). , The SBs are the "building bricks" to build the CBs, and they have no physical meaning. While the CBs represent the physical units of the model. The physical parameters for the model could be P- and S-wave velocities, density, quality factors of the medium, or some powers of these quantities.

An SB is defined by the surfaces forming the boundaries of the SB. Some boundaries may also be parts of the boundaries of the model, or fictitious extensions of boundaries. An SB may be formed by several separated regions, not only by one connected region. The division of a model into SBs is not unique. A point of the model may be situated in several SBs. The CBs are introduced to avoid a block being separated by fictitious surfaces. An CB is formed as a union of several SBs. Any point of the model must be situated in just one CB. The SBs and CBs are indexed by positive numbers, starting from 1. The system of indexing SBs and CBs may be arbitrary, but some systems may render computations more effective.

Some demo models presented in Červeny et al. [1988] are shown in Figure 16. Figure 16a shows a model with a simple layered structure. The layers are separated by non-intersecting smooth interfaces. Each layer is represented by one SB, and CBs are in this case identical with the SBs. Figure 16b shows a model of a layered structure containing an isolated body. Two different systems of indexing surfaces and SBs are used to represent the model. For example, in the middle panel of Figure 16b, the top layer is indexed by 1, the bottom layer is indexed by 3 and the surface enclosing the isolated body is indexed by 2. Therefore, the SB1 is defined by the downward side (defined as positive) of surface 1, the upward side (defined as negative) of surface 3, and the outward side (defined as positive) of surface 2. The SB2 is defined by the inward side (defined as negative) of surface 2. The SB3 is defined by the downward side of surface 3. The boundaries of SB1 and SB3 also contain parts of the boundaries of the model volume.

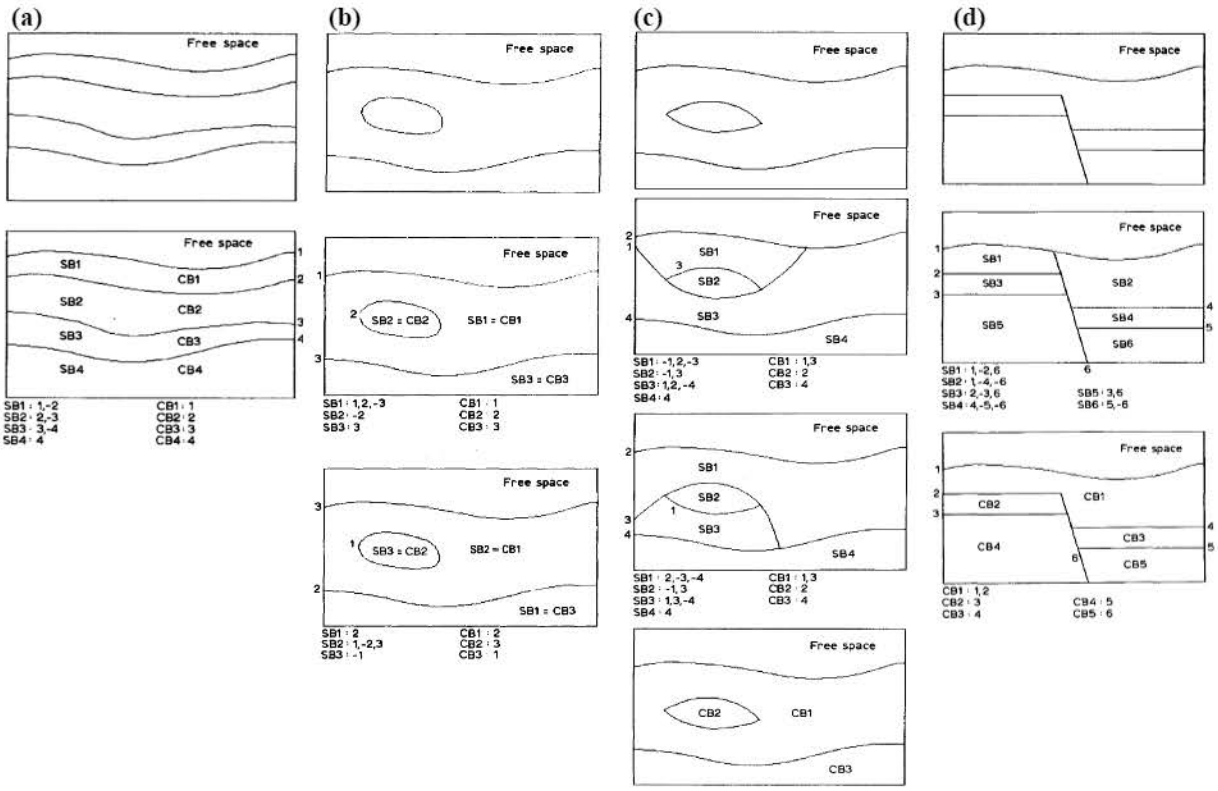

Figure 16. Four examples illustrating the method to describe 3D models in the CRT program. The figures are taken from Figure 3 – 6 in Červeny et al. [1988].

The model shown in Figure 16c looks like that in Figure 16b, but the construction method for SBs is different because the isolated body in Figure 16c has sharp (non-smooth) edges. Some auxiliary surfaces must be added by extending the actual surfaces of the block to form SBs. Two possible representations of the model in terms of SBs are shown in Figure 16c. This example shows that: (i) the division of models into SBs may be non-unique; (ii) although the region represented by SB1 and SB3 is one physical unit, it cannot be represented by one SB, but SB1 and SB3 may be united to form one CB of the same physical properties. CB2 and CB3 are identical to the SBs. Figure 16d shows a model of a simple fracture structure with a sedimentary cover. SB1 and SB2 may be united to form a CB, and the other CBs are identical with SBs. These demos show that the model construction method used in the CRT program provides great flexibility to describe any complicated 3D model.

4.3 Demo CRT Computation

We parameterize the model shown in Figure 16c and use it to perform a demo CRT computation. The model space is set in a Cartesian coordinate system, so that the covariant components, contravariant components, and Christoffel symbols are:

$$G_{ij} = \delta_{ij},\ G^{ij} = \delta^{ij},\ \text{and}\ \Gamma^{k}_{ij} = 0, \tag{6}$$

respectively. Surfaces 1 and 3 are intersected 3D surfaces, thus forming an isolated block in the model (Figure 17). Surfaces 2 and 4 have only 2D structures, and their structures along axis Y are constant. We assign distinct velocity and density values to the three CBs. Within each CB,

we assign constant values to the velocity and density, but in practice, we can also use 1D or 3D physical parameters in a CB.

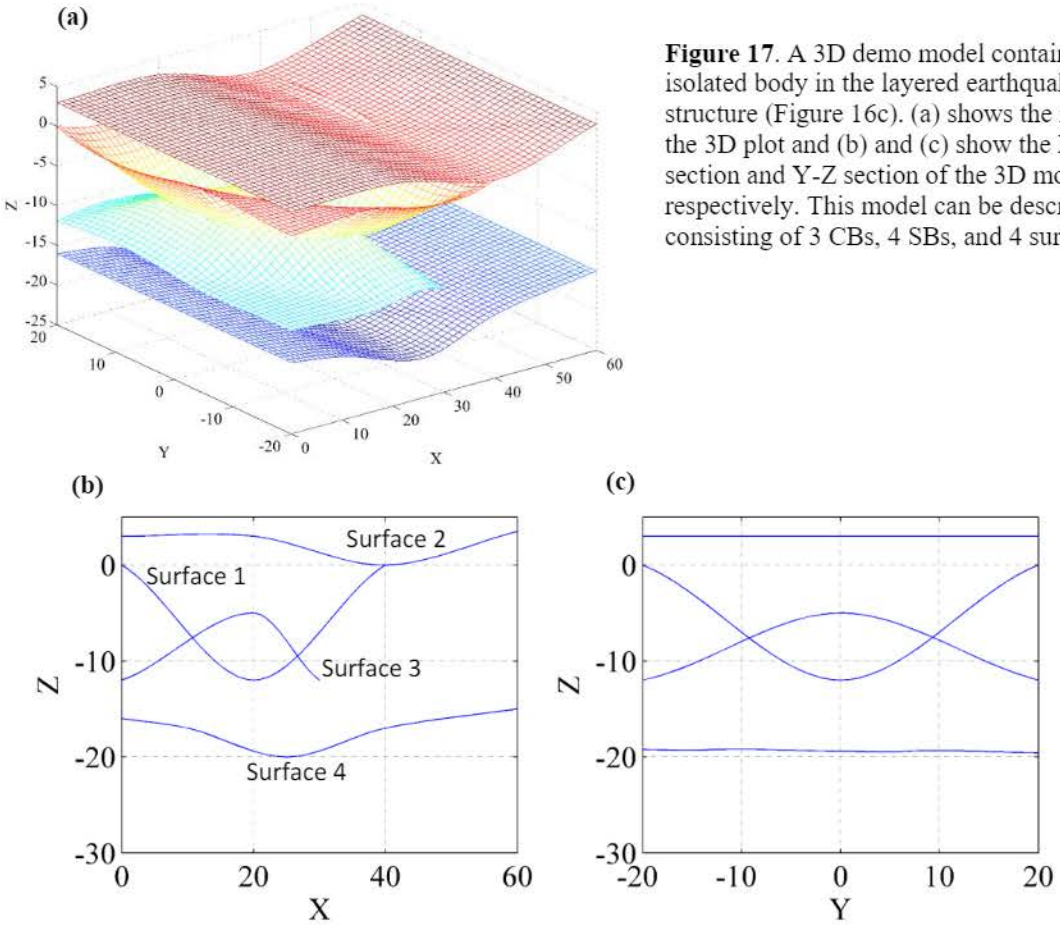

Figure 17. A 3D demo model containing an isolated body in the layered earthquake structure (Figure 16c). (a) shows the model in the 3D plot and (b) and (c) show the X-Z section and Y-Z section of the 3D model, respectively. This model can be described by consisting of 3 CBs, 4 SBs, and 4 surfaces.

The seismic ray leaving a source point can be described by azimuth and take-off angle. The CRT program has the capability of computing a group of rays by providing a range of azimuths and take-off angles. In this demo, we compute a group of rays leaving the source at [25.0, 5.0, -23.0] towards different directions (Figure 18). The azimuths are chosen from 20° to 270° with a step of 45°. Note that the azimuth in the program is measured from axis X or the east direction in geographic coordinate. It is different from the geographic definition for azimuth, which is measured from the north direction. In our computation, the take-off angles are chosen from 0° to 80° with a step of 20°, corresponding to upward seismic rays. The take-off angle is measured from horizontal. The downward rays can also be computed by assigning negative take-off angles.

Figure 18 shows the computed coordinates (blue dots) along each ray for P-wave, which are part of the output of the CRT program. To view the distribution of computed rays clearly, we plot the rays projected on X-Z, Y-Z, and X-Y sections, respectively. The coordinates of points along the ray are not always computed at the interfaces separating the blocks with different parameters. The quantities on these interfaces are output in another specified file. In the CRT program, there are many criteria to terminate the ray tracing computation, such as when a ray intersects any boundary of the model volume, overcritical transmission, S-wave in a liquid block, and zero amplitudes of reflected or converted waves. Therefore, the ray tracing computation of some rays

may be early terminated before the rays reach to the receivers on the free surface, which is usually we request.

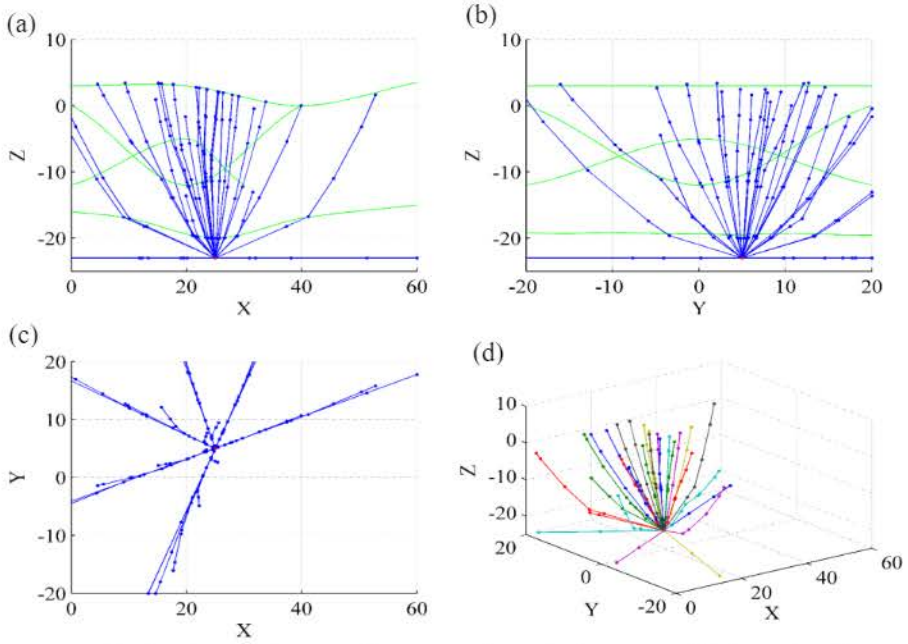

Figure 18. Computed seismic rays from a point source through the 3D model shown in Figure 13. The seismic rays leave the source with different azimuths and take-off angles. (a), (b) and (c) show the rays projecting on X-Z, Y-Z, and X-Y sections, respectively. (d) shows the rays in a 3D plot.

4.4 1D Seismic Ray Tracing Simulation

When we figure out how to set up parameters for the CRT program, we start seismic ray tracing for our problem with a 1D model. We limit the range of model space to 33.5° - 48.5° Lat, 115.5° - 140.5° Lon, and 700km deep. All the stations as well as the deep earthquakes used in this study are contained in this model space (Figure 8 and Figure 9). According to the knowledge of previous studies, the farther areas are not affected by the CBS magma reservoir. The maximum depth of the model extends to 700km because no deep earthquake we used is beyond 700km (Figure 9 and Table 1).

In the first stage, we make use of the 1D AK135 velocity model (Figure 10) to perform CRT simulations. In the 1D AK135 model, the crust consists of two layers with uniform P and S velocities. The Moho discontinuity is located at 35km. The upper mantle discontinuities are located at 410km and 660km, respectively. Between the mantle discontinuities, the velocities have a gradient structure. The land topography of the free surface is considered in building our model. The ETOPO1 global relief model [https://www.ngdc.noaa.gov/mgg/global/] within our model space is used to replace the free surface in the AK135 model. Similarly, the 3D Moho depth across the model space is also taken into account. We replace the Moho depth model shown in Figure 5 for the Moho discontinuity at 35km in the AK135 model. The crustal and upper mantle parts of our built model is shown in Figure 19. The model space is set in a geographic spherical coordinate system so that the metric tensor reads:

$$G_{ij} = \begin{bmatrix} r^2 cos^2\theta & 0 & 0 \\ 0 & r^2 & 0 \\ 0 & 0 & 1 \end{bmatrix}, G^{ij} = \begin{bmatrix} r^{-2} cos^{-2}\theta & 0 & 0 \\ 0 & r^{-2} & 0 \\ 0 & 0 & 1 \end{bmatrix}, \quad (7)$$

respectively, and the Christoffel symbols are

$$\Gamma_{ij}^1 = \begin{bmatrix} 0 & -tan\theta & r^{-1} \\ -tan\theta & 0 & 0 \\ r^{-1} & 0 & 0 \end{bmatrix}, \Gamma_{ij}^2 = \begin{bmatrix} sin\theta\, cos\theta & 0 & 0 \\ 0 & 0 & r^{-1} \\ 0 & r^{-1} & 0 \end{bmatrix}, \Gamma_{ij}^3 = \begin{bmatrix} -rcos^2\theta & 0 & 0 \\ 0 & -r & 0 \\ 0 & 0 & 0 \end{bmatrix}, \quad (8)$$

where θ is the latitude and r is the radial distance.

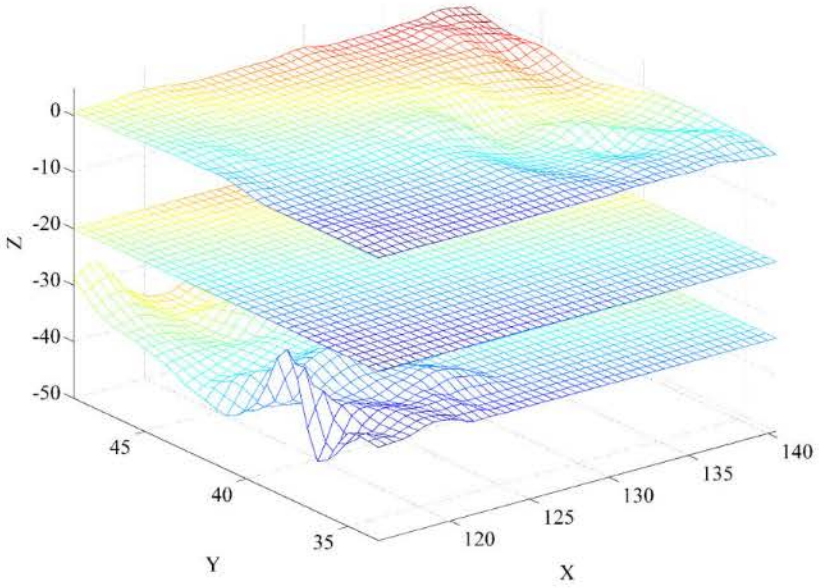

Figure 19. .3D plot of the crust and upper mantle parts of the model for ray tracing computation. The rest parts of the model are taken from the AK135 model. Our model extends to 700km deep and uses geographic coordinates. The longitude is labeled as X and the latitude is labeled as Y.

Because the CRT is a forward simulation algorithm, it can compute a seismic ray leaving a source point with prescribed azimuth and take-off angle but cannot determine the azimuth and take-off angle automatically according to the positions of the leaving point and the receiving site of the ray. We thus compute a group of seismic rays by setting a range of azimuths and take-off angles and gradually adjust the azimuths and take-off angles until the ray reaches the required receiving sites [Chen, 1998]. Figure 20 shows the ray tracing results for an earthquake 2010.02.18_01.13.184 (Table 1). The simulated rays leaving the hypocenter of this earthquake (42.59° Lat, 130.68° Lon, and 573.9km deep) with multiple azimuths and take-off angles. If the azimuths and take-off angles are dense enough, the endpoints of simulated rays can reach all used stations. In this example, the azimuth is chosen from 47° to 232° with a step of 2°. Note that the azimuth is measured from the east in the CRT program. The take-off angle is chosen from 0° to 90° with a step of 2°, which means that we compute only upward seismic rays.

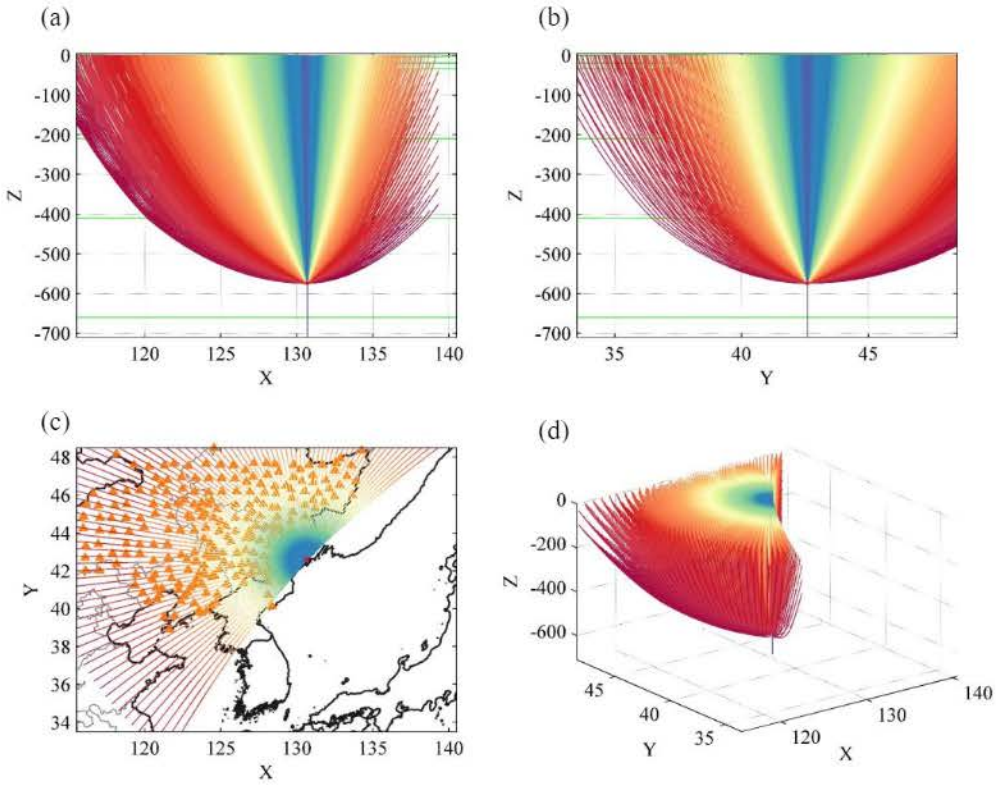

Figure 20. Computed seismic rays from the point source of the hypocenter of earthquake 2010.02.18_01.13.184 through the modified AK135 model. The seismic rays leave the source with different azimuths and take-off angles. (a), (b) and (c) show the rays projecting on X-Z, Y-Z, and X-Y sections, respectively. X corresponds to longitude and Y corresponds to latitude. The orange triangles in (c) denote stations. (d) seismic rays in a 3D plot.

The simulated seismic rays cover all used stations (Figure 20c). For each station, we search for the ray whose endpoint is closest to that station. The histogram in Figure 21a shows the distribution of the distances between a station and the closest endpoint of the found ray. Most distances are less than 30km with a minimum value of only about 2km. Based on the results of this initial ray tracing computation, we refine the range of azimuths and take-off angles for each station and perform ray tracing again for each station. Through adjusting azimuths and take-off angles and performing ray tracing several times, the computed seismic rays gradually approach each station. Figure 22 shows the rays of the earthquake 2010.02.18_01.13.184 to each station that records this earthquake. Note that the stations without seismic rays (Figure 22c) mean that they do not have usable seismograms for the earthquake. The distribution of the distances between a station and the endpoint of the computed ray for that station is plotted in Figure 21b. Comparing to the initial result in Figure 21a, we find that the distances for ~95% of stations are less than 5km. The corresponding seismic ray is thus considered as the ray reaching the station. As the hypocentral distances of this earthquake to all stations are more than 500km, this small distance between a station and the endpoint of the ray for that station is of insignificance in our further analysis.

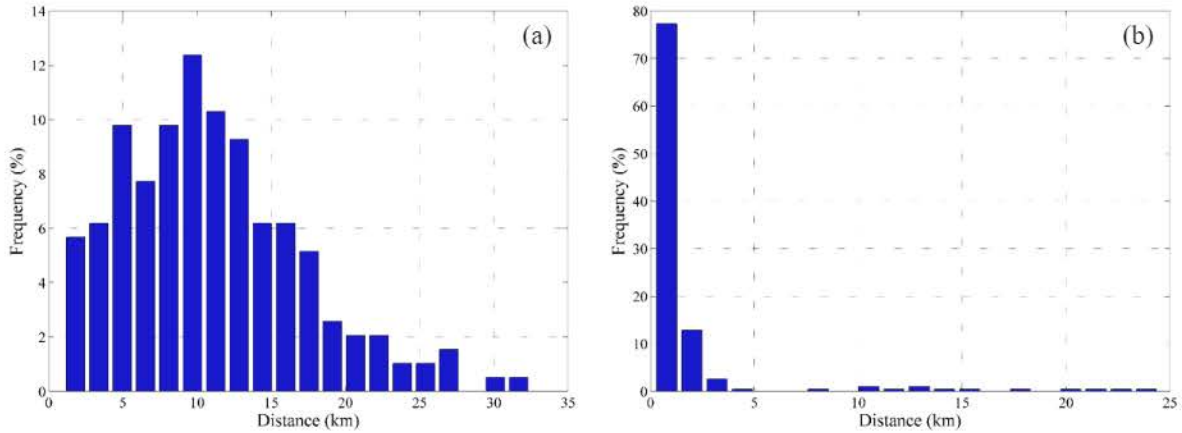

Figure 21. (a) Distribution of the distances between a station and the closest endpoint of the found rays after the initial ray tracing computation using a wide range of azimuths and take-off angles. (b) The distribution of the distances between a station and the endpoint of the computed ray for that station using refined azimuth and take-off angle.

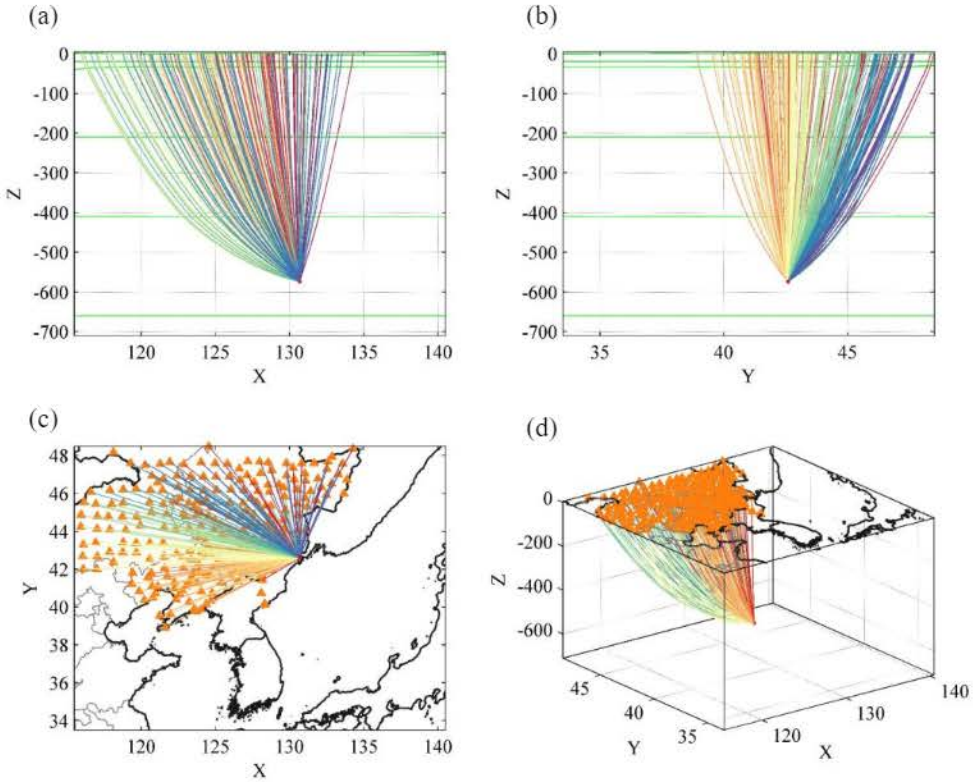

Figure 22. Same as Figure 20, but only the seismic rays reaching to the stations with usable seismograms are plotted.

For each station with the usable seismogram, we define a travel time residue as the picked P-wave time minus the predicted time computed by the CRT program. The distribution of the travel time residues for all stations is plotted in the histogram in Figure 23a. For most stations, the actual P-wave travel times are longer than the predicted times, meaning the average velocity structure in NE China is lower than the global AK135 model. An apparent feature that we can find in Figure 23a is that the travel time residues can be divided into two groups, one group is within 0 – 2s and

the other is within 3 – 5s. If we apply a local velocity model more reflecting the actual Earth structure of NE China to the ray tracing simulation, we may reduce the travel time residues by about 2s, but this cannot eliminate the residues in the second group. We plot the stations with large travel time residues between 3 – 5s in red color in Figure 23b. Most of such stations concentrate on the areas surrounding the CBS volcanic region, which means that the large travel time residues are caused by a low-velocity anomaly beneath the CBS volcano. Because the deep earthquake is located to the east of the CBS volcano, when the seismic rays of this event propagate through the low-velocity block, this block also causes large P-wave delays on all westward stations (Figure 23b).

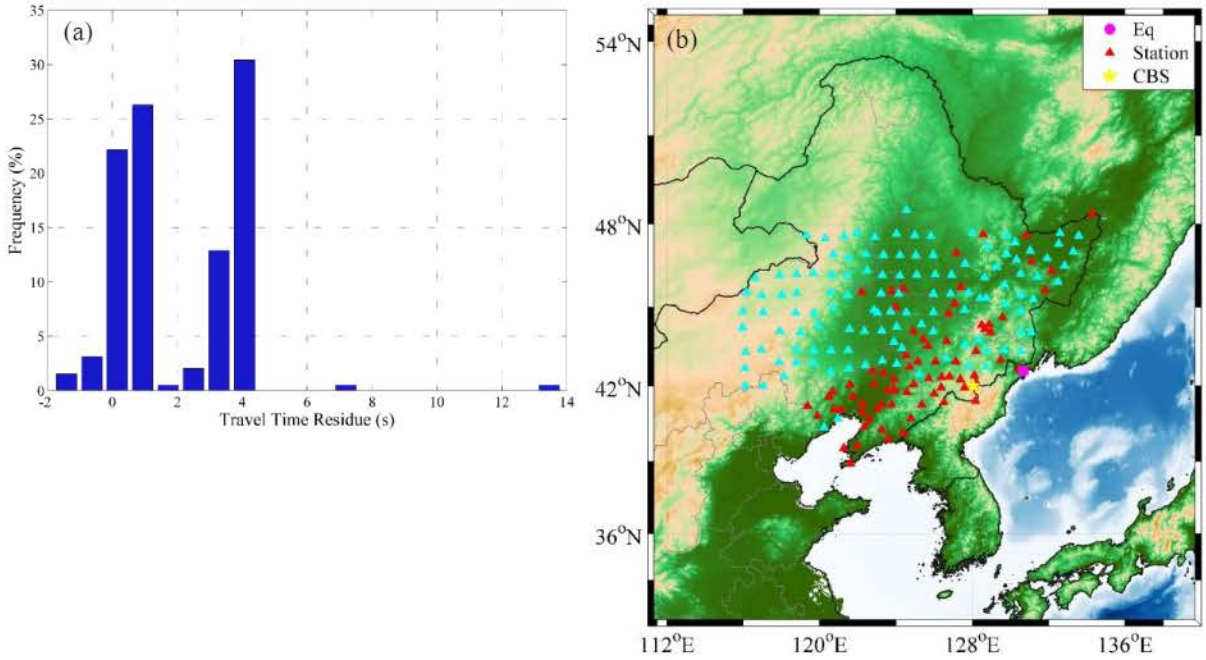

Figure 23. (a) Distribution of the time residues between picked and predicted P-wave travel times. (b) The stations whose time residues are between 3s and 5s are plotted in red colors. Other stations are plotted in cyan colors.

5 DISCUSSION, CONCLUSIONS, AND FUTURE WORK

Many previous geophysical studies provided evidence that there exists a low-velocity anomaly beneath the CBS volcano, probably corresponding to a magma reservoir in the crust and upper mantle. However, the location, range, and degree of melt of the magma reservoir indicated by previous studies are ambiguous. We propose to perform extensive ray tracing to precisely determine the properties of the CBS magma reservoir. The deep-focus earthquakes that occurred within the Wadati-Benioff seismic zone along with the subducting Pacific slab beneath the Japan Sea and the northeastern Eurasian continent margin provide good seismic sources to perform 3D ray tracing computations. The seismic rays of these deep earthquakes will fully scan the media beneath the CBS to arrive at the stations on the surface. We can determine the properties of the media beneath the CBS by adjusting these properties in performing 3D ray tracing until the predicted P- and S-wave features, such as arrival times and amplitudes, match the observations.

We select 73 deep-focus earthquakes with a minimum magnitude of 4.5 occurred from 1996 to 2017. These earthquakes are recorded at 5 temporal seismic networks (1U, XI, XL, YP, and V0) and 3 permanent seismic networks (HL, JL, and LN) deployed in NE China. Many stations in these

networks were directly located around the CBS volcano areas. In the first-year technical progress period, we process thousands of seismograms of the 73 deep earthquakes recorded on the temporal and permanent seismic networks, and manually pick P- and S-wave arrivals. During the procedure of data processing, we detect P-wave delays and S-wave shadows for many stations. All these observed P-wave delays and S-wave shadows are related to the potential magma reservoir beneath the CBS volcano. The S-wave shadow is quantified by the ratio of the S/P amplitudes. For many earthquakes, the stations showing S-wave shadows concentrate around the CBS volcanic region and extend to a large area in NE China.

The CRT program developed by Červeny et al. [1988] is a powerful tool for dynamic ray tracing simulations. In the first-year technical progress period, we spend a lot of time in understanding and configuring input parameters for the CRT program. The input parameters are organized in different input files, including constructing 3D models, specifying the type of wave (P or S), propagation direction when leaving the source and behavior at interfaces (reflection, transmission, and conversion), and controlling the numerical computation. We have performed broad tests for these input parameters using various demo models.

Next, we perform the first ray tracing simulation for our problem starting with a 1D model. Our observations along with the conclusions derived from previous studies provide us the knowledge to determine the parameters for the CRT program. The 1D global AK135 earth model is used for the CRT program, but the top free surface is replaced with the 3D topography and the Moho discontinuity is replaced with the 3D Moho depth for the area of NE China. The P-wave ray reaching each station is obtained by adjusting the azimuth and take-off angle of the seismic ray leaving the source. We show the ray tracing results of one earthquake (2010.02.18_01.13.184) propagating to all stations that record this event in this report. The results show clear P-wave delays for the stations surrounding the CBS volcanic region. The P-wave delays are as large as 3 – 5s, indicating that they are caused by a low-velocity anomaly beneath the CBS volcano. It is difficult to decide the exact location and range of this low-velocity media using only one event. We will then perform ray tracing for more earthquakes with different hypocenters in the next step. Meanwhile, we will extend the 1D model to a 3D model by inserting a low-velocity anomaly in the crust and upper mantle below the CBS volcanic region.

6 REFERENCES

Červeny, V. and Klimeš, L. (1984). Synthetic body wave seismograms for three-dimensional laterally varying media, *Geophys. J. R. astr. Soc*., 79, 119 – 133.

Červeny, V., Klimeš, L. and Psencik, I. (1988). Complete seismic ray tracing in three-dimensional structures, In: D. Doornbos (Editor), *Seismological Algorithms—Computational Methods and Computer Programs*, Academic Press, San Diego, 469.

Chen, H.-W. (1998). Three-dimensional geometrical ray theory and modelling of transmitted seismic energy of data from the Nevada Test Site, *Geophys. J. Int*., 133, 363 – 378.

Chen, Y. and F. Niu (2016). Joint inversion of receiver functions and surface waves with enhanced Preconditioning on densely distributed CNDSN stations: Crustal and upper mantle structure beneath China, *J. Geophys. Res. Solid Earth*, 121, doi:10.1002/2015JB012450.

Duan, Y.-H., Zhang, X.-K., Liu, Z., Yuan, Q.-X., Xu, Z.-F., Wang, F.-Y., Fang, S.-M. and Yang, Z.-X. (2005). Study on crustal structures of Changbaishan-Jingpohu volcanic area using receiver functions, *C. J. Geophys*., 48, 389 – 396.

Hammond, J. O. S., Wu, J.-P., Ri, K.-S., Wei, W., Yu, J.-N., and Oppenheimer, C. (2020). Distribution of partial melts beneath Changbaishan/Paektu volcano, China/Democratic

People's Republic of Korea, *Geochemistry, Geophysics, Geosystems*, 21, e2019GC008461, doi:org/10.1029/2019GC008461.

Hetland, E., Wu, F., and Song, J. (2004). Crustal structure in the Changbaishan volcanic area, China, determined by modeling receiver functions, *Tectonophysics*, 386, 157-175.

Huang, J. and Zhao, D. (2006). High-resolution mantle tomography of China and surrounding regions, *J. Geophys. Res.*, 111, B09305, doi:10.1029/2005JB004066.

Kang, T., Baag, C. and Chu, K. (2011). Volcanic eruptions and seismicity of Mt. Baekdu (Changbai) occurred in the historical time, *American Geophysical Union, Fall Meeting 2011*, Abstract ID: S51E-07.

Kennett B. L. N., Engdahl E. R. and Buland R. (1995). Constraints on seismic velocities in the earth from travel times, *Geophys. J. Int.*, 122, 108-124.

Kim, S., Tkalčić, H., & Rhie, J. (2017). Seismic constraints on magma evolution beneath Mount Baekdu (Changbai) volcano from transdimensional Bayesian inversion of ambient noise data. Journal of Geophysical Research: Solid Earth, 122, 5452–5473. https://doi.org/10.1002/2017JB014105.

Lei, J. and D. Zhao (2005). P-wave tomography and origin of the Changbai intraplate volcano in Northeast Asia, *Tectonophysics*, 397, 281– 295.

Li, Y., Wu, Q. Pan, J., and Sun, L. (2012). S-wave velocity structure of northeastern China from joint inversion of Rayleigh wave phase and group velocities, *Geophys. J. Int.*, 190, 105-115, doi:10.1111/j.1365-246X.2012.05503.x.

Lin, C.-H. (2016), Evidence for a magma reservoir beneath the Taipei metropolis of Taiwan from both S-wave shadows and P-wave delays, *Scientific Reports*, 6, 39500.

Lin, C.-H., Y.-C. Lai, M.-H. Shih and H.-C. Pu (2018). Seismic anatomy of molten sill reservoirs by both S-wave shadows and reflections, *Scientific Reports*, 8, 16401.

Liu, Z., Zhang, X.-K., Wang, F.-Y., Duan, Y.-H., & Lai, X.-l. (2005). 2-D crustal Poisson's ratio from seismic travel time inversion in Changbaishan Tianchi volcanic region, *Acta Seismologica Sinica*, 18(3), 345–353.

Qiu, G. G., Pei, F. G., Fang, H., Fang, H., Du, B. R., Zhang, X. B., et al. (2014). Analysis of magma chamber at the Tianchi volcano area in Changbai mountain, *Chinese J. Geophys.*, 57(10), 3466–3477. (in Chinese).

Ri, K.-S., Hammond, J. O. S., Ko, C.-N., Hyok, K., Yun, Y.-G., Pak, G.-J., Ri, C.-S., Oppenheimer, C., Liu, K. W., Lacovino, K., and Ryu, K.-R. (2016). Evidence for partial melt in the crust beneath Mt. Paektu (Changbaishan), Democratic People's Republic of Korea and China, *Sci. Adv.*, doi:10.1126/sciadv.1501513.

Song, J., Hetland, E. A.,Wu, F. T., Zhang, X., Liu, G., & Yang, Z. (2007). P-wave velocity structure under the Changbaishan volcanic region, NE China, from wide-angle reflection and refraction data. *Tectonophysics*, 433(1-4), 127–139.

Sun, W.-B. and He, Y.-S. (2004). The feature of seismicity in Northeast China and its relation to the subduction of the Japan sea plate, *Earthquake and Geology*, 26(1), 122 – 132.

Tang, J., Deng, Q. and Zhao, G. (2001). Electric conductivity and magma chamber at the Tianchi volcano area in Changbaishan, *Seismol. Geol.*, 23, 191–200 (in Chinese).

Tang, Y., M. Obayashi, F. Niu, S. P. Grand, Y. J. Chen, H. Kawakatsu, S. Tanaka, J. Ning and J. F. Ni (2014). Changbaishan volcanism in northeast China linked to subduction-induced mantle upwelling, Nature Geoscience, 2014, doi:10.1038/ngeo2166.

Tao, K. Liu, F. Ning, J. Chen, Y. Grand, S. Kawakatsu, H., Tanaka, S. Obayashi, M., and Ni, J. (2014). Crustal structure beneath NE China imaged by NECESSArray receiver function data, *Earth Planet. Sci. Lett.*, 398, 48-57, doi:10.1016/j.epsl.2014.04.043.

Tatsumi, Y., Maruyama, S., Nohda, S. (1990). Mechanism of back arc opening in the Japan Sea: role of asthenospheric injection, *Tectonophysics*, 181, 299-306.

Turcotte, D. L. and Schubert, G. (1982). Geodynamics, applications of continuum physics to geological problems, *John Wiley and Sons press*, New York, 44.

Wu, J., Jiao, W., Ming, Y., & Su, W. (2006). Attenuation of coda waves at the Changbaishan Tianchi volcanic area in Northeast China. *Pure and Applied Geophysics*, 163(7), 1351–1368.

Wu, J., Ming, Y., Fang, L., & Wang, W. (2009). S-wave velocity structure beneath Changbaishan volcano inferred from receiver function. *Earthquake Science*, 22, 409–416.

Yang, Y., Lei, J., Ai, Y., Zhang, G., Sun, C., Fan, E., et al. (2019). Crustal structure beneath Northeast China from ambient noise tomography. *Physics of the Earth and Planetary Interiors*, 293, 106257.

Zhang, C., Zhang, X., Zhao, J., Liu, B., Zhang, J., Yang, Z., Hai, Y., Sun, G. (2002). Crust-mantle structure of the Changbaishan Tianchi volcanic region and its vicinity: An exploratory study and inferences, *Chinese J. Geophys.*, 45, 862-871.

Zhang, M. and O'Reilly, S. (1997). Geochemical evolution of basaltic rocks from the Changbai Mountains: implications for the nature of lithospheric mantle beneath the NE margin of the Sino-Korean craton, In: Lee, Y. and Kim, J. (Eds), Tectonic evolution of eastern Asian continent, *Geol. Soc. Korea 50th Anniv. Int'l Symp.*, 170-175.

Zhao, D. and Tian, Y. (2013). Changbai intraplate volcanism and deep earthquakes in east Asia: a possible link? *Geophys. J. Int.*, 195, 706-724, doi:10.1093/gji/ggt289.

Zhu, G. Shi, Y. and Tackley, P. (2010). Subduction of the western Pacific plate underneath Northeast China: Implications of numerical studies, *Phys. Earth Planet. Int.*, 178, 92-99, doi:10.1016/j.pepi.2009.10.008.

Zhu, H., Tian, Y., Zhao, D., Li, H., & Liu, C. (2019). Seismic structure of the Changbai intraplate volcano in NE China from joint inversion of ambient noise and receiver functions. *J. Geophys. Res.: Solid Earth*, 124, 4984–5002. https://doi.org/10.1029/2018JB016600.